IDŐJÁRÁS

QUARTERLY JOURNAL
OF THE HUNGARIAN METEOROLOGICAL SERVICE

CONTENTS

****

http://www.met.hu/firat/ido-e.html

VOL. 101 * NO. 3 * JULY–SEPTEMBER 1997

IDŐJÁRÁS

Quarterly Journal of the Hungarian Meteorological Service

Editorial Office: P.O. Box 39, H-1675 Budapest, Hungary or
Gilice tér 39, H-1181 Budapest, Hungary
E-mail: gmajor@met.hu or *antal@met.hu*
Fax: (36-1) 290-7387

Subscription by

mail: IDŐJÁRÁS, P.O. Box 39, H-1675 Budapest, Hungary;
E-mail: gmajor@met.hu or *antal@met.hu*; *Fax: (36-1) 290-7387*

IDŐJÁRÁS

Quarterly Journal of the Hungarian Meteorological Service
Vol. 101, No. 3, July–September 1997, pp. 161–171

Variations and trends of land surface air temperature, 1891–1992

Zsuzsanna Iványi

Department of Meteorology, Eötvös Loránd University,
Ludovika tér 2, H-1083 Budapest, Hungary; E-mail: ivanyi@ludens.elte.hu

(Manuscript received 15 October 1996; in final form 3 January 1997)

Abstract—Long-term land surface air temperature series have been used for investigation of their variation and trends. Seasonal distribution was also considered. Besides global and hemispherical averages, sub-regions — corresponding more or less to the continents — were considered for not only long-term, but also shorter periods. For the long period significant warming trend was found for the global and hemispherical scales and also for the continents except Africa. Warming rates for some continents exceed in each season the global and hemispherical trends. Variation of trend with time revealed that no significant trend exist for the sub-periods except the last one: 1970–1992. Maximum of warming rates was found in months D-J-F on global and hemispherical scales. In these months North Asia shows extreme warming rate in the last sub-period. Relations between the warming rates for the various scales are different. Global and northern hemispherical trends correlate well, however very weak connections were found between the continents of the Northern Hemisphere.

Key-words: global warming, temperature trend, seasonal and geographical distribution.

1. Introduction

Surface air temperature variations show very different pictures on the various scales. The earlier theoretical and empirical investigations were mostly focused on global and hemispherical scales, but it has soon turned out that not only the value of the trend, but also the sign is different on regional scales. Trends of surface air temperature have widely been reported by several papers in the past using various data base with different length and spatial resolution (e.g. see *Jones et al.*, 1982; *Ghil* and *Vantard*, 1991; *Nitta* and *Yoshimura*, 1993; *Jones*, 1988 and 1994). The common finding of these studies was that the trend of the surface air temperature changed during the past 100 year. For global temperature averages a warming period was found from 1880 to 1940, then a cooling

period was observed. The duration of the cooling period is different according to the different authors. The end of this period varies between 1960 and 1970. After 1970 a warming period started again. These statements had been confirmed by the last report of *IPCC* (1996). The results mentioned above are valid for the global averages, however hemispherical, continental and regional averages show different characteristics.

Nitta and *Yoshimura* (1993) studied the trends and interdecadal variations of the global, hemispherical and continental land surface air temperature during the last 100 year period using the most available up-to-date temperature data series till 1990. A warming rate of about 0.54°C/100 years was found on global scale. However, the temperature had interdecadal variation, with the largest warming rate after 1970 up to now. Confirming former results cooling trend was found between 1940 and 1970 not only on global scale, but also in the sub-regions, but the rate was very different.

It seemed to be worthwhile to carry out a detailed investigation, to see how the surface air temperature trends changed during the past approximately 100 years on global, hemispherical and continental scale in the different seasons. The seasonal variation of the temperature trends has already been studied by some authors. *Angell* (1988) made a temperature analysis for the surface and for three upper layers using data between 1958 and 1977 for three zones of the globe. A difference was found between the temperature trends and between the seasons and it was advised to extend the analysis using the longest record available. *Jones et al.* (1982) and *Kelly et al.* (1982) studied surface air temperature trends between 1881 and 1980 for the Northern Hemisphere. All seasons showed similar long-term trends, but there were noticeable differences on time-scales of 10 years or less. Both the magnitude of the long-term trends and the year to year variability were the greatest in winter. It is confirmed by the report of *IPCC* (1996) showing that recent warming is most noticeable in winter and spring over the mid-latitude continents of the Northern Hemisphere.

For the characterization of the geographical distribution *Hansen* and *Lebedeff* (1987) used also long temperature series (1880–1985) to analyze the variation of trends. Global, hemispherical, regional (16 boxes) averages were calculated. The seasonal variation was also included, but main emphasis was taken for the yearly averages and their geographical distributions. They found that earlier warming was focused at high latitudes of the Northern Hemisphere, while recent warming is more global. *Trenberth* (1990) investigated the geographic spatial structure of the interdecadal temperature variations associated with changes in the atmospheric circulation. He found that there exist some links, but this does not rule out other external mechanism.

It is not a question that the global, hemispherical and continental surface temperature averages, furthermore their variations are very much different, i.e. the nature or character of the surface air temperature trends on various scales is still not clear. In this paper seasonal temperature trends gained for global

and hemispherical averages, furthermore for the northern and southern part of the continents are introduced and compared. The question to be answered is, what kind of relation exists between the temperature trends in the different regions of the globe. A special emphasis is put on the period following 1970, since, as it was indicated by *Nitta* and Yoshimura (1993), the highest warming trend was found in the period of 1970–1990. It is worth to recite *Jones*'s result (1988), who stated that during the period of 1967–1986 the warming was the strongest in the mid-latitudes in the Northern Hemisphere between 30° and 60°, with the exception of Europe.

2. Data base

This study is based on the same data base used by *Nitta* and *Yoshimura* (1993), except that the latest available data were also considered. The above mentioned temperature data set was provided by the Japan Meteorological Agency and includes monthly mean land air temperatures for 1881–1992. The procedure of averaging is described by *Nitta* and *Yoshimura* (1993). Briefly summarizing the procedure the main steps were as follows:

(i) Reference period was chosen to be 1951–1980.

(ii) Deviations from the monthly mean temperature average defined above had been calculated for each of the individual stations, then anomalies had been determined for each grid using a distance-dependent weighting factor measured from the center of the grid.

(iii) Mean temperature anomalies had been determined for the following 8 sub-regions: Europe, North Asia, North America, North Africa, South Asia, South Africa, Oceania, South America. Hemispherical and global averages had also been calculated.

Data used for the analyses include only land surface air temperatures. In spite of the fact that the effect of oceans is extremely important in the dynamics of the atmosphere and in the process of global warming, only land surface air temperature time series was used for these analyses in order to provide long data-series without uncertainties and avoiding difficulties due to the great number of missing data. The sporadic available temperature data over oceans and their unreliability might have caused some errors. One more thing should be stressed: Trends presented in this study might slightly overestimate the real values, since heat-island effect was not eliminated from the data. However *Hansen* and *Lebedeff* (1987) have shown that neglecting temperature data referring to big cities does not cause much change in the value of warming. The difference between the two cases is less than 10%. However, one should keep in mind that in specific areas urbanization effects may be significant (*IPCC*, 1996).

3. Data analysis

The huge amount of data had been classified according to the seasons for each subregion, the two hemispheres and the globe, as well. Since many data were missing in the period between 1881 and 1890, final analyses were executed for the period of 1891–1992. Linear regression was applied, though it requires perfect independence with time between the elements, which is not absolutely true for the temperature. Results gained by the statistical analysis can be considered as approximate indicators for the probably expectable variations of the temperature on various scales over land surfaces. Trends for the total period without considering seasons can be found in *Nitta* and *Yoshimura*'s paper (1993). On the basis of our researches seasonal trends are presented for the various scales for the whole period and for a short one lasting from 1970 to 1992. Temperature trends contained by the following tables are related to the whole- and sub-period. In the tables asterisks denote where significant trend was found. In these cases the values of temperature change show the probable warming trend with a confidence level higher than 95%.

For the whole period a significant warming trend exists for each season in most of the cases. Non-significant cases are not marked. In months of S-O-N the number of significant cases is low, which can not be explained for the time being. For significant trends it can be seen from *Table 1* that there are differences in the values of warming trends for the continents. North Asia shows the highest rate of warming, which occurred in winter (D-J-F) and spring (M-A-M). Northern Hemisphere and Europe have also high values of positive trend in the same seasons, which are higher then the annual warming rates. In the Southern Hemisphere the seasonal differences are not so marked. Altogether in D-J-F North Asia had the highest rate of temperature change, then South Africa, South America and Europe. In spring (M-A-M) North Asia is the first in the order, then comes South America, South Africa and Europe. In summer (J-J-A) an extreme warming rate was found in North America, furthermore in South America and South Africa values are higher than the global and hemispherical averages. In the months of S-O-N South America experienced the highest warming rate.

Seasonal temperature deviations from the reference period for the Northern Hemisphere is depicted in *Fig. 1* for the whole period. In the figures the circles show the length of the sub-periods. *Fig. 2*, *Fig. 3* and *Fig. 4* are the same, but for the Southern Hemisphere, North Asia and Europe, respectively. The reason for choosing North Asia is that extremely high warming rates occurred. In the Northern Hemisphere the highest rate of temperature increase was experienced in D-J-F and M-A-M. In the other two seasons the rate of change is about less than half of that (Fig 1.). In the Southern Hemisphere the rate of temperature increase varies between 0.52°C/100 yr and 0.36°C/100 yr, so the differences between the seasons are not high (*Fig. 2*). In North Asia the rate of warming

is very extreme in D-J-F and M-A-M, but similar to the global and hemispherical averages in the other two seasons (Fig. 3). In Europe the highest warming rate was found in winter and spring, but no significant warming was found in summer (Fig. 4).

Table 1. Seasonal temperature trends in °C/100 yr for the whole period (1891–1992)

Region/months	D-J-F	M-A-M	J-J-A	S-O-N
Global	*0.61	*0.59	*0.31	*0.32
Northern Hemisphere	*0.65	*0.63	*0.28	*0.29
Southern Hemisphere	*0.50	*0.52	*0.38	*0.37
Europe	*0.63	*0.67	0.17	*0.36
North Asia	*1.50	*1.20	*0.27	0.36
North America	0.23	*0.56	*0.71	0.13
North Africa	*0.28	*0.51	0.05	0.06
South Asia	*0.30	*0.35	*0.29	0.27
South Africa	*0.72	*0.68	*0.49	0.18
Oceania	0.01	*0.33	*0.27	0.17
South America	*0.69	*0.68	*0.52	*0.82

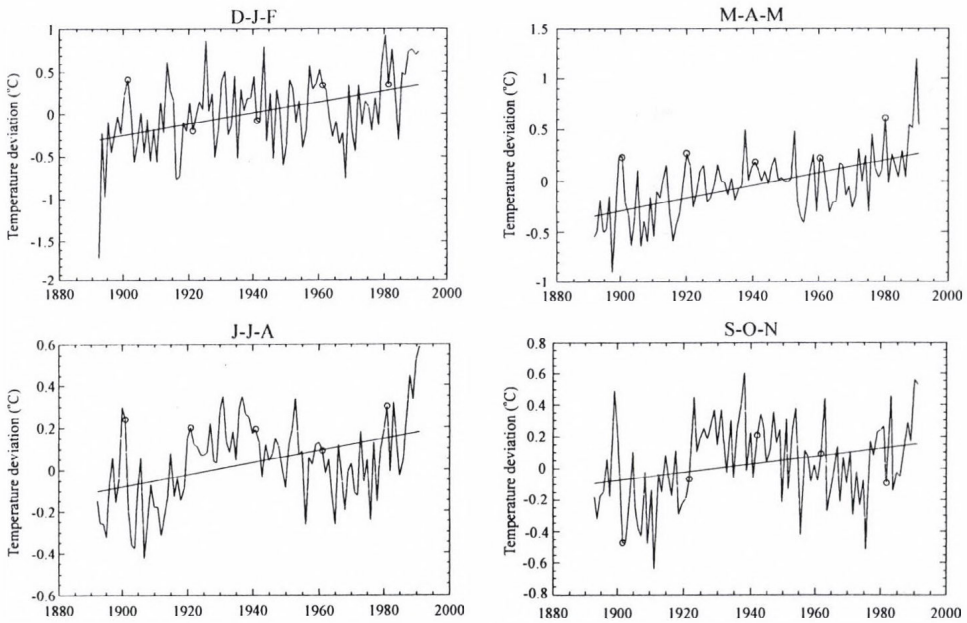

Fig. 1. Seasonal temperature deviations (°C) from the reference period (1951–1980) averages for the Northern Hemisphere.

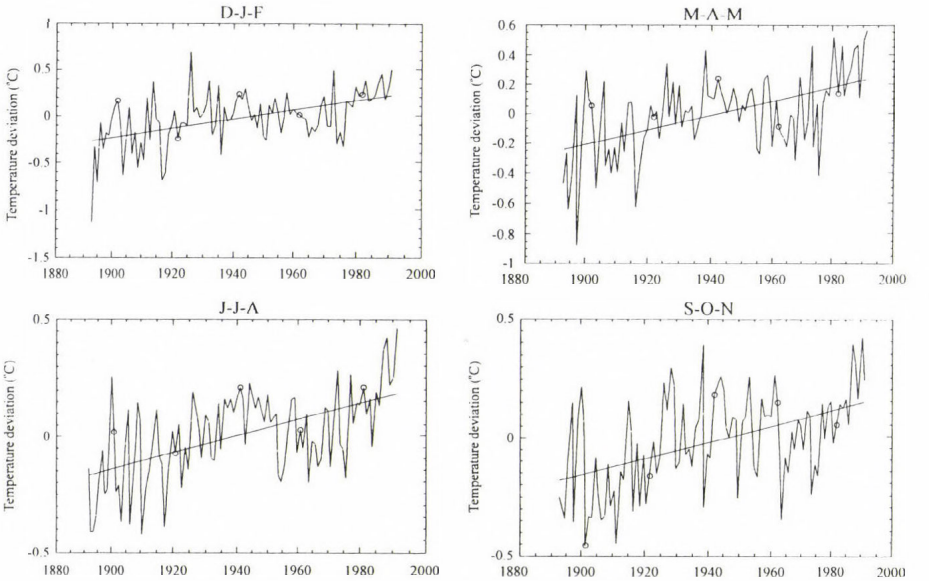

Fig. 2. Seasonal temperature deviations (°C) from the reference period (1951–1980) averages for the Southern Hemisphere.

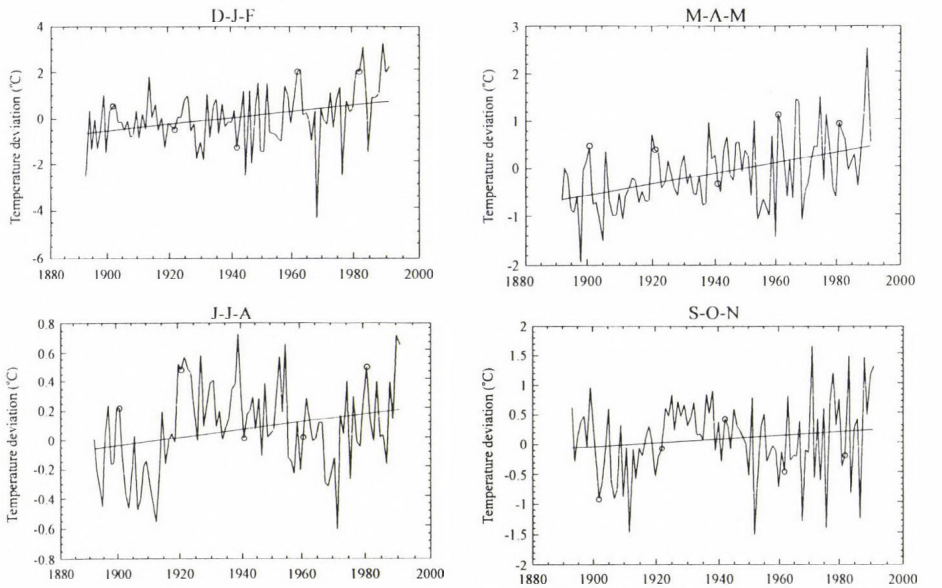

Fig. 3. Seasonal temperature deviations (°C) from the reference period (1951–1980) averages for North Asia.

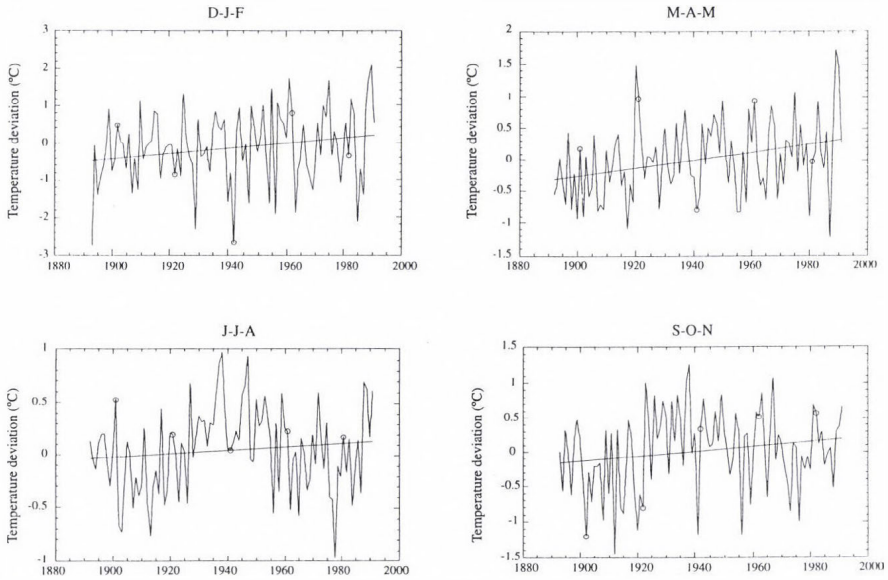

Fig. 4. Seasonal temperature deviations (°C) from the reference period (1951–1980) averages for Europe.

In the figures the differences can be seen clearly, i.e. there were warming and cooling periods in the past 100 years. For this reason trends were calculated for shorter sub-periods in order to show, how trends vary with time. The length of sub-periods was chosen to be 21 year starting from 1890, 1900 etc., so overlapping periods were considered. Very different warming and cooling rates were experienced and it can also be stated that warming rates are usually higher than those found for the total period. In the sub-periods significant trends were not found in as many cases as it was for the long period. This statement is valid for each season. *Table 2* presents calculated values of temperature change for each sub-periods for D-J-F. No significant trend exists for these short periods except the last one (1970–1992). Significant trends are marked by asterisks. North Asia has extreme value again 1.0°C/10 yr, while in other significant cases values of temperature increase vary between 0.20–0.39°C/10 yr, which are very high. South Asia and South Africa have values of 0.35°C/10 yr and 0.32°C/10 yr, respectively. These values highly exceed the warming rate received for the whole period. It has to be mentioned that in Europe no significant warming trend was found in any of the sub-periods. One more interesting thing is that in North America no significant warming rate was received even for the whole period.

Seasonal temperature trends for the last sub-period (1970–1992) are presented in *Table 3*. It is interesting that among significant cases the highest

Table 2. Temperature trends in °C/10 yr for the subperiods in D-J-F months

Region/subperiods	1890-1910	1900-1920	1910-1930	1920-1940	1930-1950	1940-1960	1950-1970	1960-1980	1970-1990	whole per.
Global	0.15	-0.09	0.11	0.03	0.08	-0.01	-0.03	-0.03	*0.34	*0.06
Northern Hemisphere	0.18	-0.08	0.09	0.04	-0.11	0.01	-0.04	-0.07	*0.39	*0.07
Southern Hemisphere	0.10	-0.09	0.17	-0.01	-0.02	-0.05	0.01	0.05	*0.21	*0.05
Europe	0.38	0.19	0.40	0.11	-0.13	0.34	-0.42	-0.08	0.15	*0.06
North Asia	0.31	0.04	-0.34	0.04	0.05	0.12	-0.15	-0.34	*1.00	*0.15
North America	0.41	-0.50	0.44	-0.14	-0.53	-0.02	-0.03	-0.19	0.57	0.02
North Africa	-0.20	0.03	0.17	-0.09	0.02	0.01	0.14	0.05	0.02	*0.03
South Asia	0.09	-0.11	0.01	0.06	-0.01	0.01	0.06	0.08	*0.35	*0.03
South Africa	-0.18	0.11	0.38	-0.02	0.02	-0.16	-0.01	-0.11	*0.32	*0.07
Oceania	-0.01	-0.08	-0.08	-0.01	0.14	0.07	0.06	0.17	0.09	0.01
South America	0.22	-0.04	0.02	0.14	-0.01	0.02	0.04	-0.07	*0.20	*0.07

Table 3. Seasonal temperature trends in °C/10 yr for the period of 1970-1992

Region/months	D-J-F	M-A-M	J-J-A	S-O-N
Global	*0.34	*0.31	*0.22	*0.19
Northern Hemisphere	*0.39	*0.33	*0.25	*0.21
Southern Hemisphere	*0.21	*0.25	*0.16	*0.16
Europe	0.15	0.24	0.14	0.23
North Asia	*1.00	0.39	*0.27	*0.29
North America	0.57	*0.40	*0.25	0.07
North Africa	0.02	*0.27	*0.33	*0.33
South Asia	*0.35	*0.29	*0.23	*0.27
South Africa	*0.32	*0.30	*0.28	*0.21
Oceania	0.09	*0.26	0.01	*0.22
South America	*0.24	*0.29	*0.13	*0.14

warming rate did not occur in winter months in every regions, e.g. in the Southern Hemisphere and South America the maximum occurs in M-A-M, not in J-J-A, which mean winter in the Southern Hemisphere. In spite of the fact that for the Northern Hemisphere significant trend exists for each seasons, it is not the same for each continent situating in the Northern Hemisphere. What can be stated is that in North America high values of temperature change occurred in the examined period in M-A-M and J-J-A, but not in the other months. In North Africa temperature increased a lot in each season except D-J-F, which was not significant. In the southern continents in most of the cases significant warming trends were found except for Oceania. However the seasonal differences are not high due to its geographical position. Comparing the two hemispherical results, it can be seen that the warming rate is higher in the north in each case.

A correlation coefficient had been determined between the rates of global, hemispherical and regional warming rates for the annual and seasonal averages. The results received for the annual averages and for the months D-J-F are summarized in *Table 4* and *Table 5*, where the comparison mostly focuses on the Northern Hemisphere, though Southern Hemisphere itself is also indicated. It can well be seen that the strongest relation exists between the global and hemispherical scales for both the annual and winter averages. Differences can be found between the correlation coefficients received for the northern continents. For the annual values North America correlates well with the global and hemispherical results. The next was found to be North Asia, then comes Europe: the correlation coefficient is only 0.559 between the Northern Hemisphere and Europe. However, the relation between Europe and North Asia seems to be stronger than that one between Europe and North America.

Table 4. Correlation coefficients between the warming rates of the sub-regions

	Global	N. Hemisph.	S. Hemisph.	Europe	N. Asia	N. America
Global	1.000	0.989	0.771	0.504	0.611	0.728
N. Hemisphere	0.989	1.000	0.673	0.559	0.651	0.734
S. Hemispere	0.771	0.673	1.000	0.122	0.298	0.499
Europe	0.504	0.559	0.122	1.000	0.476	0.154
North Asia	0.611	0.651	0.298	0.476	1.000	0.207
North America	0.728	0.734	0.499	0.154	0.207	1.000

Table 5. Correlation coefficients between the warming rates of the sub-regions for month D-J-F

	Global	N. Hemisph.	S. Hemisph.	Europe	N. Asia	N. America
Global	1.000	0.991	0.885	0.466	0.691	0.599
N. Hemisphere	0.991	1.000	0.814	0.511	0.738	0.592
S. Hemispere	0.885	0.814	1.000	0.250	0.426	0.553
Europe	0.466	0.511	0.250	1.000	0.486	0.036
North Asia	0.691	0.738	0.426	0.486	1.000	0.090
North America	0.599	0.592	0.533	0.036	0.090	1.000

4. Conclusions

Final statement can be summarized as follows:

(i) The global and hemispherical seasonal warming rates are exceeded by continental averages in each season. For the total period investigated, the following sub-regions show higher warming rates than the global and hemispherical averages: North Asia, South Africa and South America in D-J-F; North Asia, South Africa and South America in M-A-M; North America, South America and South Africa in J-J-A; South America in S-O-N.

(ii) The variation of trend with time has shown that cooling and warming periods occurred in each continent during the past 100 years. However, no significant trend was found in the sub-periods except the last one: 1970–1992. In months of D-J-F trends for the last sub-period show extremely high warming rate not only on global and hemispherical scales, but also in some regions. The seasonal variation of trend in the last sub-period shows maximum: in D-J-F on global and hemispherical scales, furthermore in North Asia, South Asia and South Africa; in M-A-M in North America; in J-J-A in North Africa; in S-O-N in North Africa.

(iii) The relations between warming trends for the various scales are very much different. Global and northern hemispherical trends correlate well, however the relations between the warming rates for the Northern Hemisphere and some continents (North America, North Asia) are not so remarkable. Very weak connection was found between the warming trends of the Northern Hemisphere and Europe. The same statement can be made for the correlation coefficients between Europe, North America and North Asia.

Finally it can be stated that the variability of the temperature change has a remarkable geographical and seasonal distribution. A very high and significant warming rate was found in the period of 1970–1992, however the relation between the warming trends for the various scales can not be explained. It means that the reason, i.e. the ratio of natural and anthropogenic factors influencing the variation of temperature, is still not clear.

Acknowledgements—The work has been supported by the Centre for Climate System Research, University of Tokyo during the author's visit in the Centre. The author wishes to extend her thanks for the support to the Centre, to *Prof. T. Matsuno*. Thanks are also extended to *Dr. Nitta*, *Dr. Nakajima* and *Dr. Baik* for their assistance.

References

Angell, J.K., 1988: Variations and trends in tropospheric and stratospheric global temperatures, 1958-87. *Journal of Climate 1*, 1296-1313.

Ghil, M. and *Vantard, R.*, 1991: Interdecadal oscillations and the warming trend in global temperature time series. *Nature 350*, 324-327.

Hansen, J. and *Lebedeff, S.*, 1987: Global trends of measured surface air temperature. *J. Geophys. Res. 92*, 13,345-13,371.

IPCC, 1996: *Climate Change 1995. The Science of Climate Change*. Contribution of Working Group I to the Second Assesment Report of the IPCC. Eds.: *J.T. Houghton, L.G. Meira Filho, B.A. Callender, N. Harris, A. Kattenberg* and *K. Maskell*. Cambridge University Press, Cambridge, U.K.

Jones, P.D., Wigley, T.M.L. and *Kelly, P.M.*, 1982: Variations in surface air temperatures: Part 1. Northern Hemisphere, 1881-1980. *Monthly Weather Review 2*, 59-70.

Jones, P.D., 1988: Hemispheric surface air temperature variations: recent trends and an update to 1987. *Journal of Climate 1*, 654-660.

Jones, P.D., 1994: Hemispheric surface air temperature variations; a reanalysis and update to 1993. *Journal of Climate 7*, 1794-1802.

Kelly, P.M., Jones, P.D., Sear, C.B., Cherry, B.S.G. and *Tavakol, R.K.*, 1982: Variations in surface air temperatures: Part 2. Arctic regions, 1881-1980. *Monthly Weather Review 2*, 71-83.

Nitta, T. and *Yoshimura, Y.*, 1993: Trends and interannual and interdecadal variations of global land surface air temperature. *J. Meteorol. Soc. Japan 3*, 367-375.

Trenberth, K.E., 1990: Recent observed interdecadal climate changes in the Northern Hemisphere. *Bull. Amer. Meteorol. Soc. 71*, 988-993.

IDŐJÁRÁS

Quarterly Journal of the Hungarian Meteorological Service
Vol. 101, No. 3, July–September 1997, pp. 173–179

Finite Markov model of long-term variations of precipitation

B. G. Vager[1] and **N. K. Serkov**[2]

[1]*Department of Calculating Mathematics,*
St. Petersburg State University of Architecture and Civil Engineering,
198005, 2nd Krasnoarmeiskaya, 4, St. Petersburg, Russia,
E-mail: BVager@compmath.abu.spb.ru

[2]*State Hydrological Institute,*
199053, 2nd liniya, V.O., 23, St. Petersburg, Russia

(Manuscript received 20 March 1996; in final form 3 January 1997)

Abstract—The finite Markov chain as a simple, robust and adequate model of long-term variations of hydrometeorological elements is suggested. The main mathematical foundations are given. Proposed techniques are illustrated with an example of annual precipitation series. The results of numerical experiments are in good agreement with observed data.

Key-words: Markov chain, factorization of state-continuous stochastic process, long-term variations, precipitation, wet (dry, normal) periods.

1. Introduction

At present mathematical methods and computers are widely used in all applied sciences including hydrometeorology. Therefore, the choice of an adequate and convenient mathematical technique is a problem of importance.

In this paper, we deal with the finite Markov chains which are convenient and effective tools for several concrete cases. The main construction in the theory of Markov chains is the transition matrix $\mathbf{P} = (p_{ij})$ whose elements are the conditional probabilities of process transitions from one state to another at the next moments. (Also, complex Markov chains may be considered. In this case a probability of current state j is suggested to be depending on k preceeding states $i_1, i_2, \ldots, i_k$, where $k > 1$.) There are many statistical criteria to decide if the given random sequence is a Markov chain or not (see, e.g. *Vager* and *Serkov*, 1995).

Reasonable classification of hydrometeorological processes, states and data for estimating transition probabilities are necessary to construct the finite Markov model. In an early stage of finite Markov chain applications the quality aspects of hydrometeorological phenomena such as synoptic positions, types of atmospheric circulation, wet and dry days etc. (*Sarymsakov et al.*, 1947; *Gabriel* and *Neumann*, 1962; *Weiss*, 1964) were analyzed.

On the other hand, finite Markov chain $C_m(t)$ with m states $\{1,2,\ldots,m\}$ can be obtained as a result of factorization of state-continuous stochastic process $X(t)$:

$$C_m(t) = i \quad \text{if} \quad a_{i-1} < X(t) \le a_i \quad (i = 1,\ldots m; \quad t = 0,1,\ldots), \tag{1}$$

where $a_0, a_1,\ldots, a_m$ are defined by the investigator:

$$-\infty = a_0 < a_1 \ldots < a_m = \infty.$$

This approach was used by *Babkin* and *Serkov* (1974). Authors suggested to consider the annual river runoff as a finite Markov chain. The values a_i can be chosen depending on the aim of the investigation. It should be considered that the number of states can not be too large. This number is limited by data available to estimate the transition probabilities.

Finite Markov chains have some advantages in comparison with other stochastic models (*Jeffers*, 1981):

(1) They are easy to construct based on experimental data.
(2) Profound knowledge of internal mechanisms of process under consideration is not required. Moreover, the analyses of models may reveal those aspects where such knowledge is important.
(3) The results of modeling may be easily presented in graphical form.
(4) The expense of computer time is not too much.

It may be added that "roughness" of finite models leads to statistical persistence (robustness) (*Huber*, 1981) of obtained estimators. It is especially important in case of short time series.

The main limitations are the sufficient volume of initial information required for statistical significant estimation of transition probabilities and independence of functional mechanisms of process in question.

The above mentioned items are considered in a monograph (*Serkov* and *Vager*, 1995) in more details.

Specific mathematical aspects of the Markov chain theory are considered in special mathematical literature (see e.g. *Romanovskiy*, 1949; *Feller*, 1957; *Aivazyan*, 1975; *Billingsley*, 1961) but not in this paper. Our aim was to illustrate how a relatively simple mathematical tool gives important climatological information.

Most of the valuable algorithms are coded in FORTRAN-77 in a program package for personal computers.

2. *Mathematical foundations*

For solving agrometeorological and other economical problems it is important to estimate the statistical properties of dry and wet periods.

A year is considered wet if the annual precipitation exceeds a given critical value, dry if it is less than another critical value and normal in between. It corresponds to the case $m = 3$ in Eq. (1).

The transition matrix is (p_{ij}) $(i,j = 1,2,3)$, where indices "1", "2" and "3" means dry, normal and wet states, respectively.

The matrix (non-stochastic) of corresponding standard deviations is denoted by (s_{ij}) $(i,j = 1,2,3)$, as

$$s_{ij} = [p_{ij}(1 - p_{ij})/n_i]^{1/2}, \tag{2}$$

where n_i is the number of state "i" (*Romanovskiy*, 1949).

Dry (wet, normal) period of length n is a sequence of n dry (wet, normal) years defined by non-wet (-dry, -normal) years at both sides. It is easy to show (see e.g. *Feller*, 1957) that the probability of the dry period having the length of n is equal to

$$Pn(1) = p_{11}^{n-1}(1 - p_{11}), \tag{3}$$

where $p_{11} = Pr\{1 \mid 1\}$ is the corresponding conditional probability. The mean length $n_m(1)$ of the dry period is equal to

$$n_m(1) = (1 - p_{11})^{-1}. \tag{4}$$

Similar formulae hold for normal and wet periods.

3. *An example*

The time series of annual precipitation amounts at the meteorological station of Cola (Murmansk region, Russia) during the years 1897–1981 was chosen for a numerical experiment (*Fig. 1*).

The mean of value EX is equal to 431 mm, standard deviation s = 94 mm. The critical values a_1 and a_2 in Eq. (1) were chosen as a_1 = EX - 0.5 s = 394 mm, a_2 = EX + 0.5 s = 478 mm.

Transition probabilities were estimated by the maximum likelihood method (*Romanovskiy*, 1949) resulting in the formula

$$p_{ij} = n_{ij}/n_i, \tag{5}$$

where n_{ij} is the number of transitions from "i" to "j", n_i is the sum of n_{ij}. The transition matrix obtained is

$$\begin{matrix} 0.40 & 0.32 & 0.28 \\ 0.33 & 0.43 & 0.24 \\ 0.09 & 0.59 & 0.32 \end{matrix}$$

and corresponding standard deviations (2) are

$$\begin{matrix} 0.10 & 0.09 & 0.09 \\ 0.08 & 0.08 & 0.07 \\ 0.06 & 0.10 & 0.10 \end{matrix}$$

It is evident that the values p_{ij} twice and more times larger than their standard deviations s_{ij}.

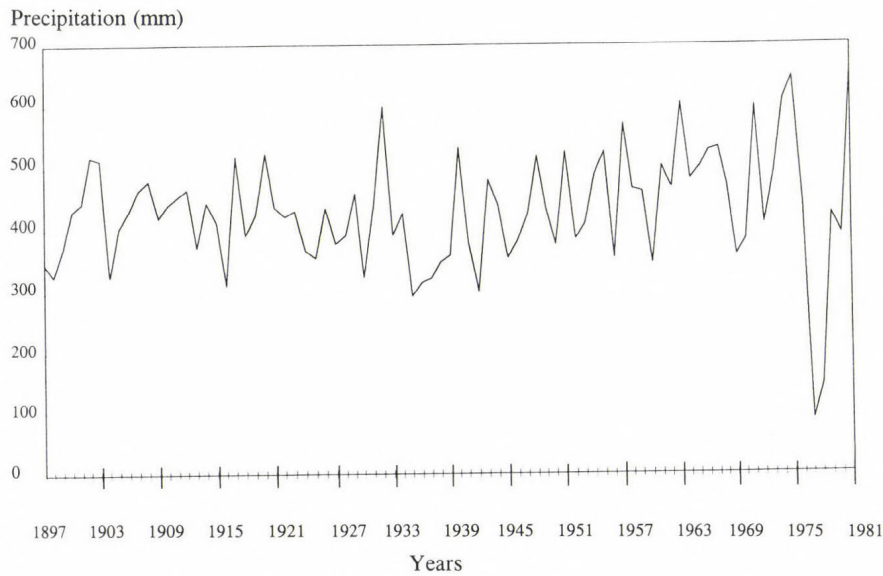

Fig. 1. The time series of annual precipitation at meteorological station Cola between 1897–1981.

The probability distribution of lengths of dry, normal and wet periods calculated with Eqs. (3) and (4) are presented in *Table 1*. (The datum in numerator is corresponding to formulae (3) and (4), and the one in denominator is corresponding to the empirical estimator.)

There is a good fit of the model to experimental values.

Table 1. The probability distribution of lengths of periods

i	1	2	3
p_{ii}	0.40	0.43	0.32
$P_1(i)$	0.60 — 0.60	0.57 — 0.48	0.68 — 0.80
$P_2(i)$	0.24 — 0.27	0.24 — 0.33	0.22 — 0.07
$P_3(i)$	0.10 — 0.07	0.11 — 0.14	0.07 — 0.07
$P_4(i)$	0.04 — 0.00	0.05 — 0.05	0.02 — 0.00
$P_5(i)$	0.02 — 0.07	0.02 — 0.00	0.01 — 0.07
$n_m(i)$	1.67 — 1.70	1.75 — 1.76	1.47 — 1.50

4. Concluding remarks

The long-range fluctuations of such hydrometeorological elements as runoff, precipitation, evaporation, air temperature and others were investigated in many papers reviewed by *Vager* and *Serkov* (1995). Among these investigations, the works of scientists of the State Hydrological Institute (St. Petersburg, Russia) are to mentioned especially (*Babkin* and *Serkov*, 1974; *Babkin et al.*, 1984; *Vuglinskiy et al.*, 1986; *Voskresenskiy et al.*, 1977; *Plitkin*, 1987; *Rumyantzev* and *Bovikin*, 1985 and others). The general conclusion is that results of these papers are in good accordance with prior ideas about long-range fluctuations of hydrometeorological elements.

The comparison of two models describing groups of years with low and high runoff was carried out by Serkov (see *Vager* and *Serkov*, 1995). These models were the two-states Markov chain and continuous-states *Ratkovich* (1976) models. It was shown that finite Markov chain parameters may be estimated more objective and statistically reliable. Moreover the former model leads to results which are corresponding better to available data.

Serkov (1991) developed existing method for statistical treatment of hydrological time series when zero values are in presence in order to take into

account the dynamic of a process in question. The author worked out a mixed Markov model combining the gamma-distribution and a constant equal to zero. So, the problem pointed out by *Kartvelishvili* and *Korganova* (1972) has been solved.

There are many ecological problems solved by the use of finite Markov chain techniques, i.e. weather forecasts, evaluation of atmosphere and runoff pollution, water supply, estimation of probability characteristics of low runoff periods etc. (see, e.g. *Romanof* and *Elekesh*, 1977; *Romanof* and *Tumanov*, 1993; *Serkov*, 1989 and others).

Kashyap and *Rao* (1976) note that more rough, more aggregative, more simple stochastic models may be in better accordance with experimental data in case of complex physical processes than too sophisticated models.

References

Ayvazyan, S.N., 1975: Statistical analyses of Markov chains (in Russian). Moscow.

Babkin, V.I. and *Serkov, N.K.*, 1974: Modeling of hydrological characteristics using Markov chains (in Russian). *Meteorology and Hydrology,* No. 7, 55-59.

Babkin, V.I., Vuglinskiy, V.S. and *Yudina, V.K.*, 1984: The regularities of long-range fluctuations of input and level at the Lake Baikal (in Russian). In *Hydrology of the Lake Baikal and other Reservoirs*. Novosibirsk, 110-118.

Billingsley, P., 1961: *Statistical Inference for Markov Processes*. Univ. Chicago Press, Chicago.

Feller, W., 1957: *Introduction to Probability Theory and its Applications*. 2d edition, New York. Wiley & Sons, London, Chapman & Hall.

Gabriel, K.P. and *Neumann, J.*, 1962: Markov chain model for daily rainfall occurrence at Tel-Aviv. *Quart. J. Royal Metal. Soc. 88*, No. 375, 90-95.

Huber, P.J., 1981: *Robust Statistics* (in Russian). Mir, Moscow.

Jeffers, J.N.R., 1981: *An Introduction to System Analysis: with Ecological Applications* (in Russian). Mir, Moscow.

Kartvelishvili, N.A. and *Korganova, N.S.*, 1972: Modern problems of stochastic hydrology (in Russian). *Water Resources 3*, 147-160.

Kashyap, R.L. and *Rao, A.R.*, 1976: *Dynamic Stochastic Models from Empirical Data*. Academic Press, New York.

Plitkin, G.A., 1986: Investigation of some regularities of forming and long-range river runoff resources fluctuations (in Russian). *Geography and Natural Resources 4*, 56-67.

Ratkovich, D.Ya., 1976: Long-term fluctuations of river runoff (in Russian). Gidrometeoizdat, Leningrad.

Romanov, N. and *Elecesh, N.*, 1977: On statistical dependence and robustness of some meteorological conditions having influence on an air pollution (in Russian). In *Meteorological aspects of atmospheric pollution,* Part 2, Leningrad, 80-85.

Romanov, N. and *Tumanov, S.*, 1993: Adapted Gaussian plume model characteristics and space-time structure of the estimated SO_2-concentration field due to elevated sources. *Időjárás 97*, 99-111.

Romanovskiy, V.I., 1949: *Discrete Markov Chains* (in Russian). Gostekhizdat, Moscow.

Rumyantzev, V.A. and *Bovikin, I.V.*, 1985: *Space-time Regularity in Runoff Fluctuations of Eurasian Rivers*. Nauka, Leningrad.

Sarymsakov, T.A., Dgordgio, V.A. and *Bugaev, V.A.*, 1947: On the weather formation at Central Asia (in Russian). *Reports of the USSR Acad. of Sci. 58*, 1949-1952.

Serkov, N.K., 1989: Finite Markov models (applications in hydroecology and the package of applied programs). *Theses of Coordinational Conference on Mathematical Modeling in Hydroecology*. Leningrad.

Serkov, N.K., 1991: Mixture Markov model of long-term fluctuations of periodically interrupted minimal river runoff (in Russian). *Transactions of the State Hydrological Institute, 355*, 72-76.

Vager, B.G. and *Serkov, N.K.*, 1995: *Finite Markov Chains in Meteorology and Hydrology* (in Russian). SPbGASU, St. Petersburg.

Voskresenskiy, K.P., Ivanova, I.B., Denisov, A.P. and *Savchenko, O.G.*, 1977: Water resources of the Trans-Caucasus (in Russian). *Transactions of the State Hydrological Institute*, 241, 88-98.

Vuglinskyi, V.S., Babkin, V.I., Gronskaja, T.N. and *Titova, T.E.*, 1986: On long-range characteristics computation of input to the main USSR HES reservoirs (in Russian). *Meteorology and Hydrology 8*, 89-93.

Weiss, L.L., 1964: Sequences of wet and dry days described by a Markov chain model. *Monthly Weather Rev. 92*, 169-176.

IDŐJÁRÁS

Quarterly Journal of the Hungarian Meteorological Service
Vol. 101, No. 3, July–September 1997, pp. 181–197

Acid rain in a squall line system in the Taiwan area: A numerical experiment

Ching-Sen Chen, Chuan-Yao Lin, Zen-Sing Deng and **Jing-Shiou Chen**

Institute of Atmospheric Physics, National Central University, Chung-Li, Taiwan, R. O. C.; E-mail: tchencs@storm.atm.ncu.edu.tw

(Manuscript received 12 April 1996; in final form 3 February 1997)

Abstract—In Taiwan acid rain has become one of the major environmental issues. The Environment Protection Administration of the Republic of China has set up ten stations around Taiwan island since April 1990. The average pH values from 1990 to 1994 indicated that a pH value of less than 5.0 was found in northern Taiwan where Taipei city and some industrial areas were located. As well, a station was set up in the mountainous area of central Taiwan away from both city and industrial areas, since April 1994. The mean pH value in April and May was 4.84. A cloud model with a terrain following coordinate system was used to simulate a squall line system which occurred in the Taiwan area. The model squall line passed through a polluted area where SO_2 and particulate dry sulfate were released. pH value was calculated following *Hegg et al.* (1984) and *Rutledge et al.* (1986) where the squall line system interacted with SO_2 and particulate dry sulfate. Simulation results indicated that the distribution of acid precipitation associated with the squall line system was influenced by the internal flow structure of the squall line system and the SO_2 and initial particulate sulfate profiles specified. Acid precipitation could be transported up to 100 km downstream following the precipitation system.

Key-words: acid rain, squall line, numerical study.

1. Introduction

The problem of acid rain has become one of major public concerns. Many research work has indicated that acid precipitation is widespread in Europe, in the northern United States and in southern China (*Likens* and *Bormann*, 1974; *Galloway et al.*, 1982; *Zhao et al.*, 1988). In Taiwan acid precipitation has emerged as a subject of increasing public attention since the living standard has increased so quickly. Some studies have indicated that precipitation with a pH value of less than 5 is very common on the western side of Taiwan island (*Sun* and *Wu*, 1980; *Lu et al.*, 1985). In order to obtain a better understanding of the

characteristics of acid rain in the Taiwan area, the *EPA* (Environment Protection Administration of the Republic of China) has, since April, 1990, set up ten stations (*Fig. 1*) around Taiwan island. Precipitation samples were collected automatically if precipitation occurred.

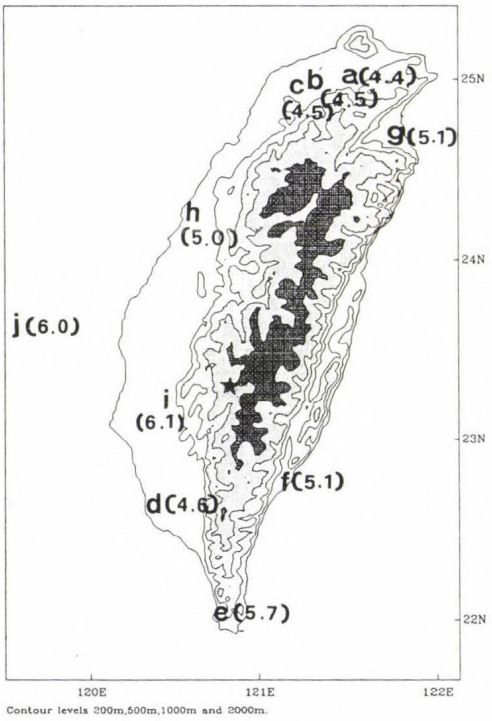

Fig. 1. The average pH value (inside the parenthesis) from April 1990 to March 1994 at ten stations (a through j) around Taiwan island. ★ denotes the mountain station set up in 1994.

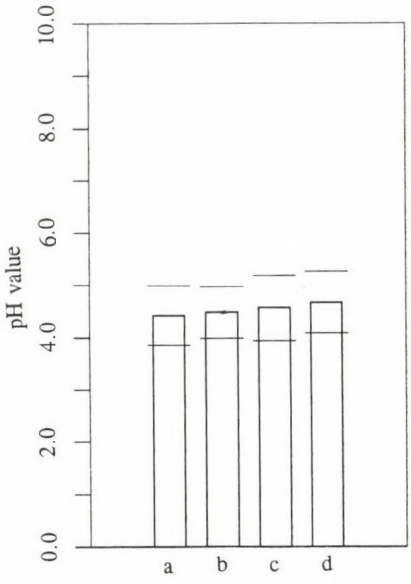

Fig. 2. The average pH value and standard deviation at stations: (a) Taipei, (b) Kuesan, (c) Chungli, (d) Kaohsiung.

The average pH value from April 1990 to March 1994 is shown in Fig. 1. pH values of less than 5.0 existed in northern Taiwan (Taipei, Kuesan and Chungli) and southern Taiwan (Kaohsiung). pH values of less than 4.0 in northern Taiwan were not unusual (*Fig. 2*). Taipei is the largest city in Taiwan and Kuesan, Chungli and Kaohsiung are the industrial cities. The pH values at the other six stations were larger than 5.0. The molar ratio of the $[SO_4^{2-}/NO_3^-]$ varied from 1.75 to 3.5 at those four sites. Thus sulfate was a major component of the acidity of precipitation in the Taiwan area. In order to find the pH value

in mountainous areas a station was set up, after April, 1994, in the Central Mountain Range about 100 km away from cities or industrial areas. The mean pH value in April and May was 4.84. A lower pH value can be found in eastern United State (pH value less than 4.2; *National Research Council*, 1983) and southern China (pH value about 4.0 in 1982/1984, Zhao et al., 1988). Thus the low pH value of acid precipitation in Taiwan is comparable to the values of these countries.

Taiwan is located near to southern Mainland China. As Mainland China is one of the major sources of SO_2 in Asia (*Akimoto* and *Narita*, 1994), the effect of SO_2 from Mainland China on acid rain in the Taiwan area cannot be ignored. However, Taiwan is also a source of SO_2 (*Akimoto* and *Narita*, 1994). Thus, the acid rain in Taiwan is certainly influenced by local sources. Therefore the first step to understand the characteristics of acid rain was to investigate how the locally released SO_2 influenced the pH value in a precipitation system. Another objective in this study was to see whether acid precipitation could occur about 100 km downwind of the polluted area. The precipitation system chosen in this study was a squall line system observed in northern Taiwan during the Taiwan Area Mesoscale Experiment (TAMEX) in 1987 (*Kuo* and *Chen*, 1990). Squall line systems usually occurred in the Taiwan area in spring every year (*Deng* and *Chen*, 1980). The squall line system that occurred in 1987 was well investigated by some studies (*Wang et al.*, 1990; *Lin et al.*, 1990; *Chen*, 1991). It was orientated in a north-south direction and propagated generally eastward from the Taiwan strait toward the island. Over the Taiwan strait, a front to rear inflow prevailed at all levels on the front side of the convective regions, while a shallow rear to front flow entered from the back of the squall line. New cells formed along the gust front in front of the squall line system and propagated into the squall line, thus prolonging the life time of the squall line. Its detailed structure was analyzed by *Wang et al.* (1990) and simulated by *Chen* (1991). Finally it became weaker in the mountain areas. In Wang et al., an area with radar reflectivity higher than 20 dBZ was found below 5 km, which corresponded to the melting level estimated from environmental sounding (*Fig. 3*). The maximum reflectivity was about 45 dBZ. In Chen's study, the basic dynamic of the squall line system did not differ substantially whether the ice phase microphysics was included or excluded. Thus we would not include ice phase microphysics in the current study of the first approximation. Here we try to use a dynamic model, including terrain, to simulate this squall line system numerically. Then we want to study the pH value in this squall line system when it passes through the polluted area in a numerical model. SO_2 and particulate sulfate were specified as the pollutants in the model. The interaction of SO_2 and particulate sulfate with cloud and rain obtained from a dynamic model produced sulfate and then the pH value could be calculated. Through this study we hope that we can attain a better understanding of the characteristics of pH values in a squall line system in the Taiwan area.

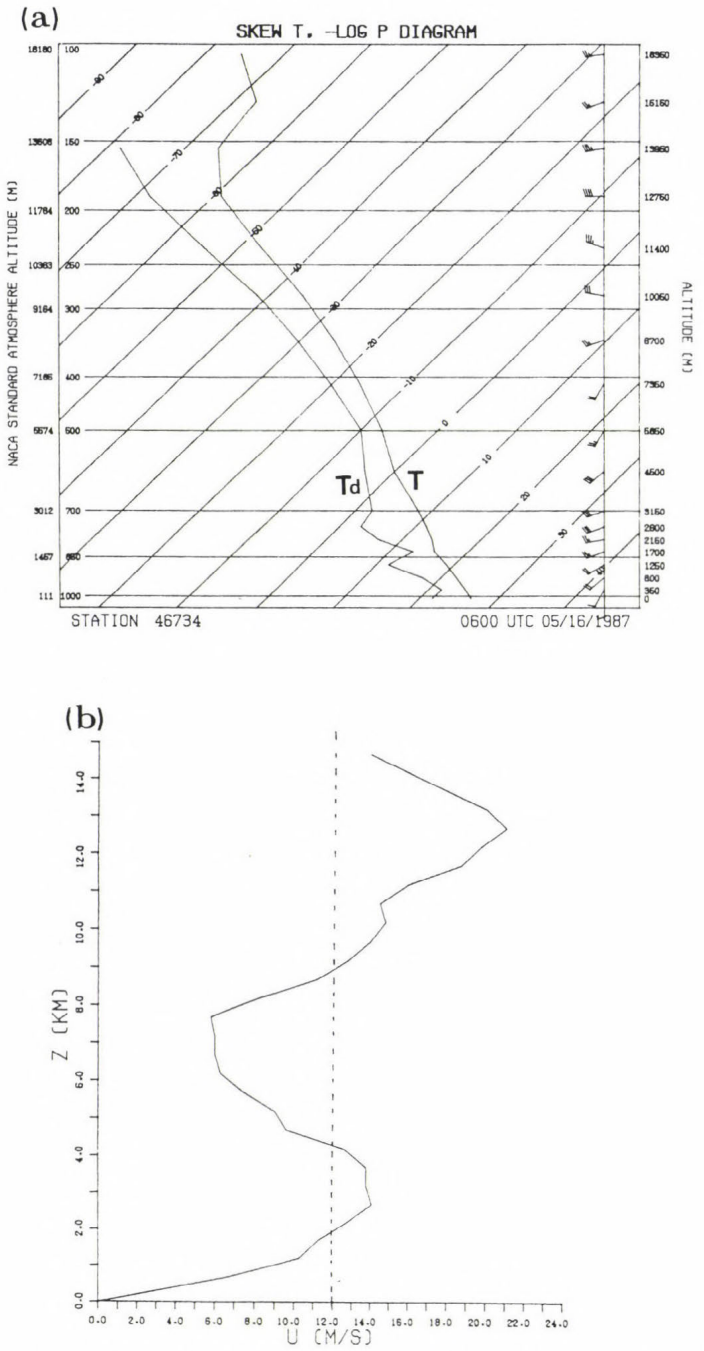

Fig. 3. (*a*): The initial temperature (T), moisture (T_d) and (*b*): wind profiles used in the model.

2. *Numerical simulation*

2.1 A brief description of the numerical model

A two-dimensional terrain-following coordinate cloud model was used to investigate orographic effects on the characteristics of a precipitation system moving from the plain toward the mountain. This model has been described in all the details by *Durran* and *Klemp* (1982). It was a two-dimensional version of *Klemp-Wilhelmson*'s (1978) cloud model with a terrain-following coordinate system introduced. In addition, a wave-absorbing layer was added to the top of the domain. Our study retained the same cloud and rainwater variables as in the Klemp-Wilhelmson model.

The base of the domain ($Z = 0$) and the surface pressure were assumed to be 0 m and 1000 hPa, respectively. The grid size in the x direction was constant and was taken to be 1.0 km, while in the z direction it was stretched vertically to allow for finer resolution in the lower atmosphere. There were 451 and 30 grid points in the horizontal and vertical directions, respectively. The time step was 4 seconds.

The model domain was 450 × 18.9 km. An 8.3 km thick sponge layer was assumed at the top of the model. The horizontal velocity, vertical velocity, non-dimensional pressure perturbation, potential temperature, and subgrid-scale mixing coefficient and the mixing ratio of water vapor, cloud water, and rainwater in the vertical direction were determined at levels whose locations are shown in *Table 1*. A more detailed description of the dynamic model structure is presented in the Appendix. The initial temperature, moisture conditions and the initial wind profile for the simulation are shown in Fig. 3. Their locations in the vertical direction for the terrain-following coordinate system were calculated by

$$\eta = \frac{Z_t (Z - Z_s)}{Z_t - Z_s},$$

where Z_t was the top of the domain (18.9 km). The terrain features (Z_s) used in the model are shown at the bottom of *Fig. 4*. The highest peak was 1.5 km in height at $x = 260$ km. Initially the observed east-west wind component was assigned everywhere in the model above the mountain top. Below the mountain peak, the wind gradually increased over 1.5 h from zero to the observed value of the sounding. Meanwhile, all the prognostic variables were integrated forward except for cloud and rain. Then we let the model adjust itself by integrating forward without considering any microphysical processes for another hour. The model time was reset to zero. At this time, low-level cooling was applied in a region 40 km away from the left boundary. This cooling area was 10 km wide and 3.8 km deep. The cooling rate was 0.01 K sec^{-1} and lasted for 10 minutes. All the parameters were taken from *Chen* (1991) in order to initi-

Table 1. The location of variables in the vertical direction. Vertical velocity is located at the ZRW position and all other variables are located at the ZRT position

Level	P (hPa)	ZRT(m)	ZRW (m)
30	71	18485	18031
29	83	17582	17138
28	96	16698	16263
27	112	15834	15409
26	129	14989	14573
25	148	14163	13758
24	169	13357	12961
23	192	12570	12184
22	216	11803	11426
21	242	11055	10688
20	269	10326	9969
19	298	9617	9270
18	329	8928	8590
17	360	8257	7929
16	393	7606	7288
15	428	6975	6666
14	463	6363	6064
13	500	5770	5481
12	538	5197	4918
11	577	4643	4374
10	616	4109	3849
9	656	3594	3344
8	697	3098	2858
7	738	2622	2391
6	779	2165	1944
5	821	1728	1516
4	861	1310	1108
3	902	911	719
2	942	532	350
1	981	173	0

alize the simulated squall line systems in the model. Then, a series of cells formed and moved eastward toward the mountainous area. The characteristics of the formation of series of cells were observed by *Wang et al.* (1990). Fig. 4 shows the maximum radar reflectivity in a vertical column varying with time. The radar reflectivity was derived from the mixing ratio of rain according to the model of *Fovell* and *Ogura* (1988). Over the plane area, the characteristics of radar reflectivity were similar to that in *Chen*'s results (1991). The precipitation over the top of the mountain was due to the lifting effect from the mountain on the moist air. At 120 min. the front edge of the squall line system was near to 140 km. Then we assumed there was a region of SO_2 located some distance

ahead of the squall line system (*Fig. 5*). The profiles for SO_2 were similar to *Hegg et al.* (1984) as follows:

$$q_{SO_2}(x,z,t=0) = q_{SO_2}(x_0,0)\, e^{-R/R_0} e^{-z/H} - q_{th},$$

where $q_{SO_2}(x,z,t=0)$ was the initial mixing ratio of SO_2 in the model, $q_{SO_2}(x_0,0)$ was the mixing ratio of SO_2 on the surface at $x = x_0$ km, H was the scale height, R_0 was the specified horizontal distance and R was the distance from (x_0) to any point in the model, horizontally. The q_{SO_2} was set to zero if it was negative. q_{th} was the threshold for q_{SO_2} being held in a specified area. Beyond this specified area, no pollution existed initially. Here we assumed that q_{th} was 10 μg kg^{-3}. Besides, R_0 and H were assumed to be 5 km. SO_2 was released in the model instantaneously. Then the interaction of the cloud and rain with q_{SO_2} was mainly taken from *Hegg et al.* (1984) and *Rutledge et al.* (1986). The interaction of solid precipitation particles with SO_2 in *Hegg et al.* and *Rutledge et al.* was not considered here, due to the secondary role of ice phase microphysics on the dynamic structure of the squall line system. The concentration of H_2O_2 and O_3 were also adapted from *Hegg et al.* as the profiles for H_2O_2 and O_3 were not available in Taiwan. The profiles for particulate sulfate were assumed to be similar to that of SO_2.

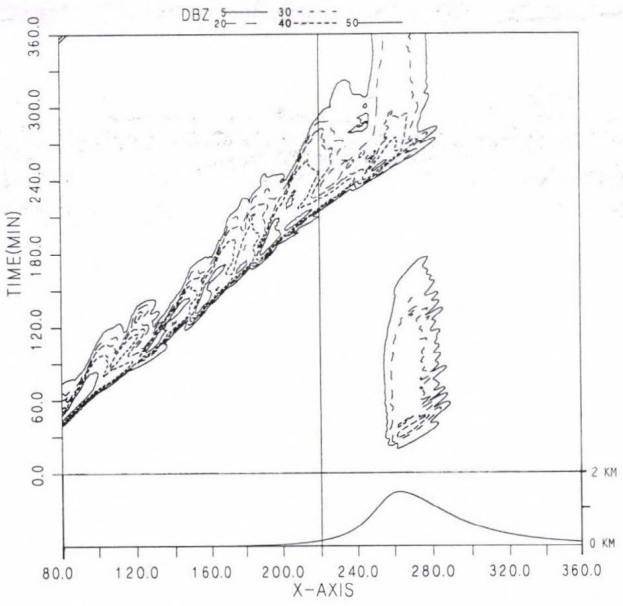

Fig. 4. The maximum radar reflectivity in a vertical column derived from the model results. The contours are 5, 20, 30, 40 and 50 dBZ. The terrain features used in the model are shown at the bottom of the figure.

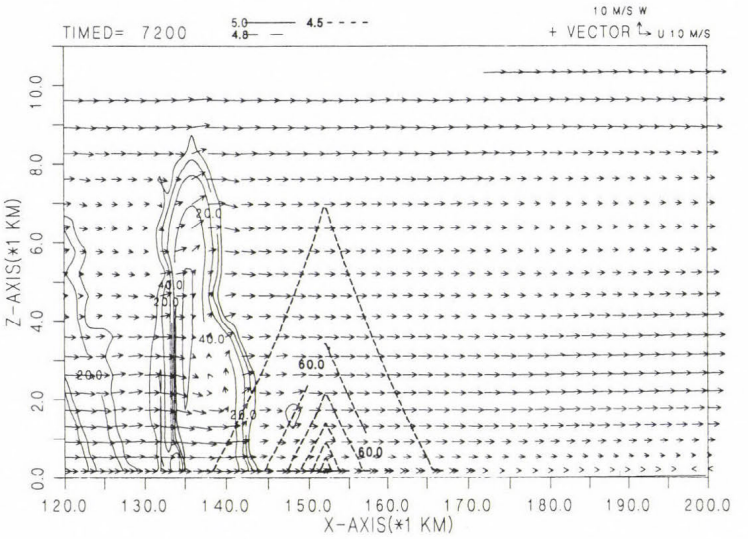

Fig. 5. The vertical cross section of radar reflectivity (solid line, contour intervals, 10 dBZ) and the mixing ratio of SO_2 (contour intervals, 50 μg kg^{-3}) at 120 min. of model time. The wind vectors relative to the ground are superimposed on the figure.

2.2 Simulation results

Seven initial q_{SO_2} profiles were considered. In experiment A, we assumed that the air was highly polluted. x_0 was assumed to be 151 km. It was about 8 km ahead of the front edge of the squall line at 120 min. (Fig. 5). q_{SO_2} was 393 μg kg^{-3} ($\approx$ 150 ppb) and no particulate sulfate was initially specified. In Taiwan the maximum daily average of SO_2 could reach this value in the industrial area (*EPA*, 1991). The 150 ppb value also appeared in Guiyang city in Mainland China (*Zhao et al.*, 1988). However 75 ppb of SO_2 (maximum daily average) could be found in the metropolitan area in Taiwan (*EPA*, 1991). The monthly mean sulfate was 8 (15) (μg kg^{-3}) for the metropolitan (industrial) area (*EPA*, 1991).

Since the formation of the new cell was in front of the squall line, the movement of the squall line system (14 m s^{-1} in the plain area) was faster than the environmental wind below 9 km in height, shown in Fig. 3. (*Wang et al.*, 1990, *Chen*, 1991). The whole squall line system could catch SO_2 originally, ahead of the squall line. The interaction of cloud and rain with SO_2 ahead of the squall line occurred first in a new cell at x near to 165 km at 150 min. (*Fig. 6a*). A region of rain water with a pH value of less than 5.0 extended upward. This was because part of the SO_2 in the low level was transported upward in the updraft area. Part of the SO_2 flew into the squall line system from the

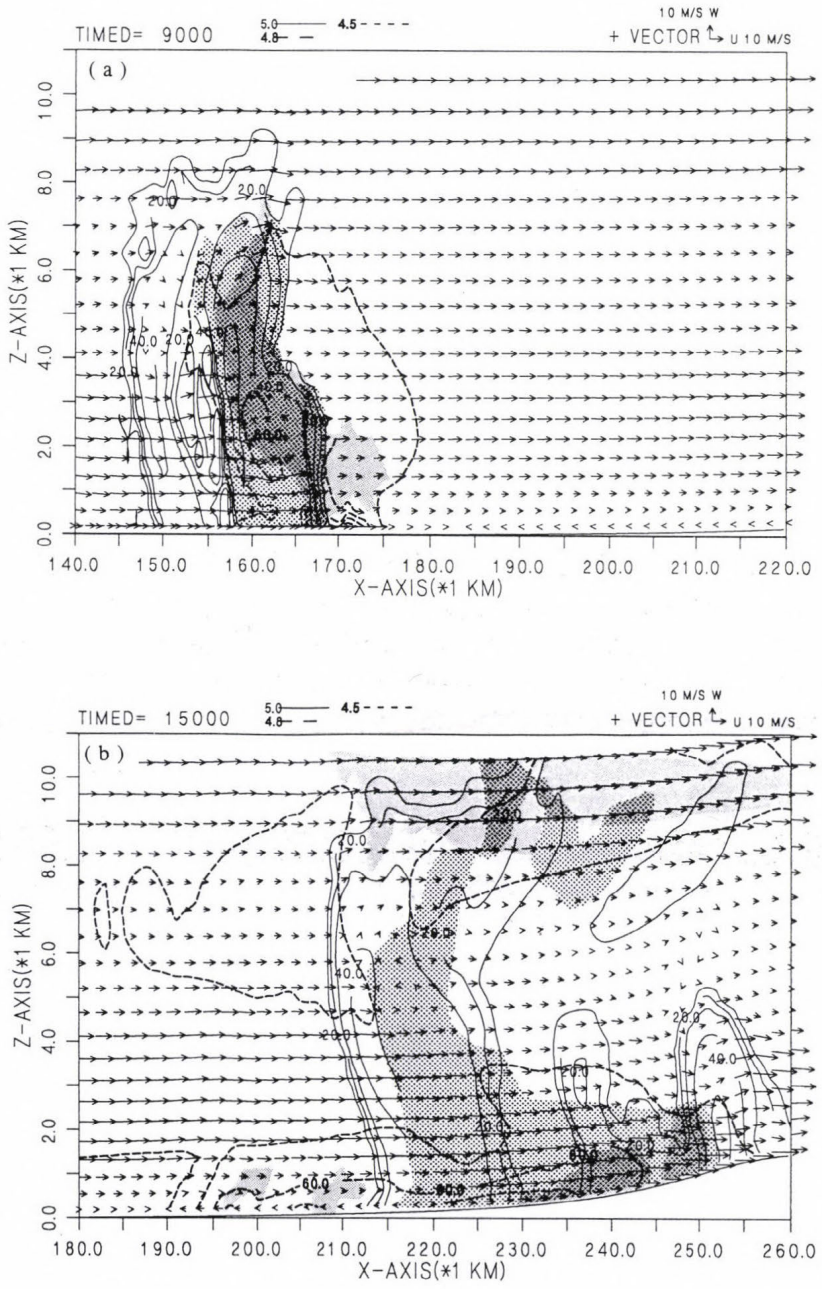

Fig. 6. The vertical cross section of radar reflectivity and mixing ratio of SO_2 like in Fig. 5. The shaded and dotted area represent the area with a pH value of less than 5.0 in both cloud and rain water, respectively. (*a*) 150 min. (*b*) 250 min.

forward side due to an inflow from the front relative to the squall line system (*Wang et al.*, 1990; *Chen*, 1991). This could help the formation of acid precipitation in the upper level. At this time some SO_2 was still located ahead of the squall line system. The acid rain area was about 10 km wide. The pH value in the cloud water had a similar pattern (Fig. 6a) but extended upward and backward from a low level near to the front side of the squall line following the airflow. As the squall line system moved toward the mountain slope at 220 min., most of the SO_2 was inside the precipitation area at the low level (figure not shown here). Some SO_2 was transported upward and backward from the squall line system. This was due to low level air flowing into the squall line from the front and going upward and backward relative to the squall line (*Wang et al.*, 1990; *Chen*, 1991). Thus part of the SO_2 was present on the backside of the squall line system in the upper level. Therefore acid precipitation with a pH value of less than 5 existed in the whole squall line system. The downdraft associated with the high reflectivity area could help the SO_2 to move downward toward the low level and spread toward the front and back sides. The area with a pH value of less than 5 in the cloud water could be found at the upper level as well as at the low level due to the existence of cloud and SO_2 in these two areas (figure not shown here). At 250 minutes of the simulation, the squall line system over the mountain slope became weaker. This was because the new cell in front of the squall line system did not grow strong enough to prolong the squall line system, while the old cell dissipated. Most of the SO_2 was traveling with the squall line system concentrated at the low levels (*Fig. 6b*). Low level SO_2 could not be transported upward easily due to the weak updraft. Therefore SO_2 moved with the airflow along the mountain slope and the horizontal area of acid rain increased. This acid rain region could extend toward the mountain when the squall line system moved over the mountain.

Fig. 7 indicates the variation of the minimum pH in rain water in a vertical column over time, for experiment A. A region with a pH less than 4.6 could extend from $x = 150$ km (where the initial q_{SO_2} was located) toward the mountain top. While areas with a pH less than 4.4 could extend 70 km from the plain toward the mountain slope. Before 180 min. the area with a lower pH value was located in the central part of the precipitation system where a high concentration of SO_2 and intensive rain were located (Fig. 6a). After 180 min. the area with a lower pH value was located on the front edge of the precipitation system, as intensive rain was found there (Fig. 6b). In experiment B, x_0 was changed to 161 km from experiment A more than 10 km distant from the squall line. It was designed to see how the separation distance between the pollution source and the precipitation system affected the property of the acid rain. Since the maximum q_{SO_2} initially specified was further away from the precipitation system, the pH value was slightly higher than in experiment A, but the pattern was similar (figure not shown). An area with a pH value of less than

4.6 could extend 60 km toward the mountainous slope areas, and a 4.7 pH value area could move further inland toward the mountain top. In experiment C, H was decreased to 2.5 km from experiment A. This meant that more SO_2 was concentrated near to the surface. The minimum pH in the vertical column was similar to the values of experiment A (figure not shown). In experiment D, the initial q_{SO_2} was reduced to 75 ppb with no sulfate specified initially. The pattern was similar to that in experiment A (Fig. 7) but the minimum pH value was higher in experiment D. An area with a pH value less than 4.7 could extend from $x = 150$ km near to the plain toward the mountain top. In experiment E, the initial SO_2 was assumed to be a quarter of the 393 μg kg^{-3} (or 38 ppb) but with no sulfate initially. The simulation results (figure not shown here) indicate that a pH value of less than 4.7 (4.8) could extend 40 km (70 km) downstream from $x = 150$ km. A pH value of less than 4.9 could be found in the sloped area half way to the top of the mountain.

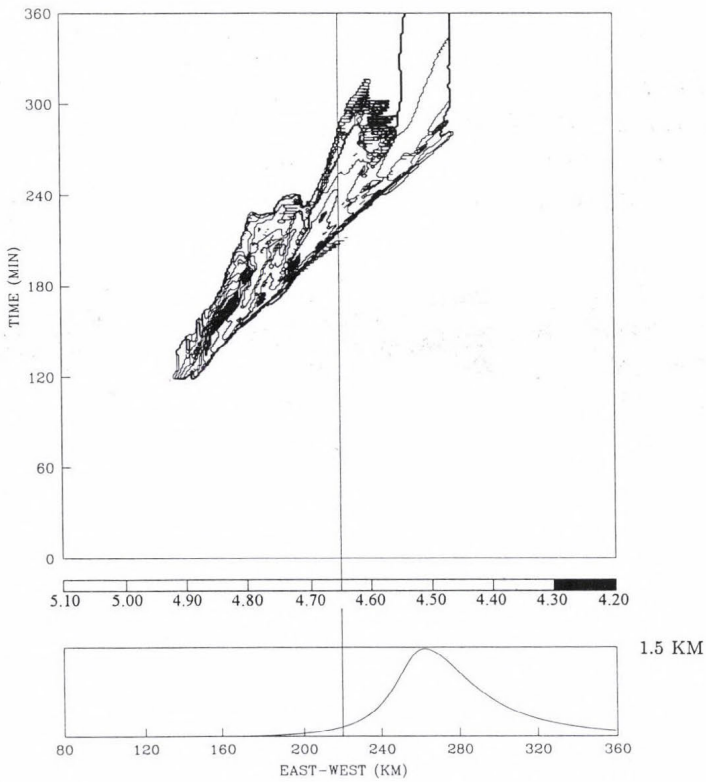

Fig. 7. The minimum pH value in a vertical column varying with time for experiment A. The various pH values are denoted by the different colors with the darker representing the lower pH value. The terrain features used in the model is shown at the bottom of the figure.

The experiment F is similar to experiment E but with additional particulate sulfate initially, with the maximum value of 10 μg kg^{-3}. The sulfate profile was the same as for SO_2. The minimum pH value in rainwater in a vertical column (*Fig. 8*) was similar to that in experiment E, but the pH value could be less than 4.6 near $x = 150$ km where the sulfate was released and near $x = 200$ km. No significant difference was found further away. The last experiment (experiment G) was designed to investigate the characteristics of acid precipitation when the model squall line encountered the "background" distribution of SO_2 and particulate sulfate. The distribution of background SO_2 and particulate sulfate were similar to that in *Hegg et al.* (1984) but the maximum value (near to the surface) of SO_2 and particulate sulfate were 20 μg kg^{-3} and 6 μg kg^{-3}, respectively. *Fig. 9* shows the minimum pH value in a vertical column over time, for experiment G. The minimum value for this case was similar to that in the previous one. But the area covered by pH value less than 5.0 was smaller in experiment G. This difference was attributed to the transportation of higher concentration of SO_2 to the back side of the squall line system in the previous case.

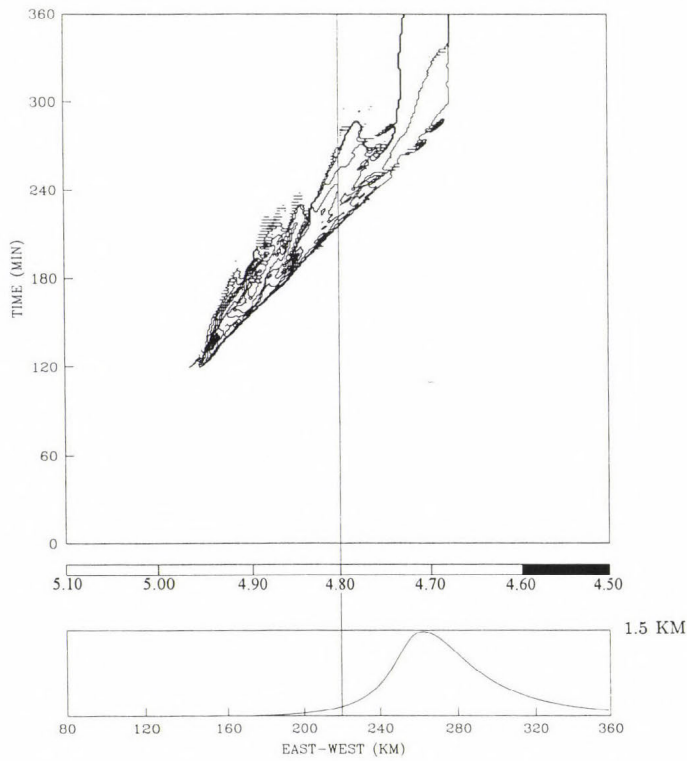

Fig. 8. Similar to Fig. 7 but for experiment F.

These seven experiments indicated that the pH value inside the squall line system was influenced by the internal flow structure and the distribution of both SO_2 and particulate sulfate. The lowest pH value in rain was strongly affected by the maximum of SO_2 concentration, particulate dry sulfate. Acid precipitation could be transported downstream over 100 km away from the pollutant area following the precipitation system. Thus acid rain occurring in mountainous areas in Taiwan was not unusual.

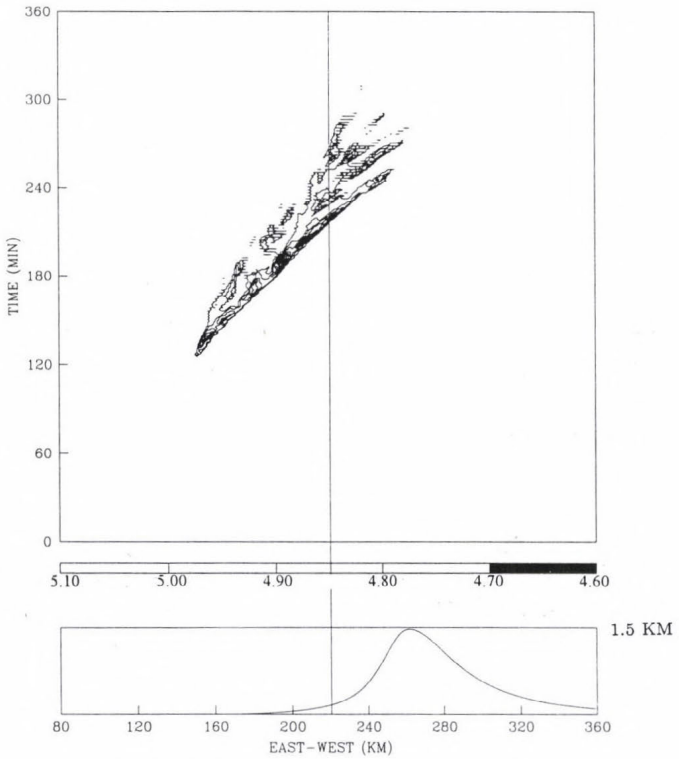

Fig. 9. Similar to Fig. 7 but for experiment G.

3. Conclusion

From ten stations around Taiwan island, we found that pH values of less than 5.0, averaged from four years of data (April 1990 to March 1994), existed at four stations. These four stations were either in Taipei, the largest city in Taiwan, or in industrial areas. A numerical model was employed to investigate the acid rain in a squall line system when it was assumed to pass through a

polluted area. Six different initial SO_2 and particulate sulfate profiles were assumed. These were determined by the maximum concentration of SO_2 or dry sulfate, the scale height of the SO_2 and sulfate, and the relative position of SO_2 and sulfate to the squall line system. The characteristics of acid rain inside the squall line system were influenced by the internal flow structure and the initial profiles of SO_2 and particulate sulfate. The decrease of the concentration of SO_2 by one-half and one quarter, the minimum pH value increased from 4.2 to 4.4 and 4.6, respectively. The initial particulate dry sulfate decreased the pH value near the source region. Acid precipitation could be transported 100 km downstream following the precipitation system.

In the future we will study the characteristics of acid rain in different precipitation systems in different seasons. The air flow inside the precipitation systems especially needs to be explored, either by observation or by simulation. Understanding the flow structure could help us to know the transportation effects of pollution on acid rain. Besides, the improvement of the dynamic and chemical model is also a very important task. For example, we need to consider nitrogen compounds in our chemical model to evaluate their effects on acid rain. To upgrade the observation data related to the acid rain is another challenge at the same time.

Acknowledgements—The reviewers' comments and suggestions were highly appreciated. This work was supported by the Environment Protection Administration of the Republic of China, under Grants EPA-83-E3F1-09-04. The computer resources were supplied by the Institute of Atmospheric Physics, National Central University, Chung-Li, Taiwan, R. O. C.

References

Akimoto, K. and *Narita, H.*, 1994: Distribution of SO_2, NO_x and CO_2 emissions from fuel combustion and industrial activities in Asia with $1° \times 1°$ resolution. *Atmospheric Environment 28*, 213-225.

Chen, C.-S., 1991: A numerical study of a squall line over the Taiwan strait during TAMEX IOP\#2. *Mon. Wea. Rev. 119*, 2677-2698.

Deng, Z.-S. and *Chen, C.-S.*, 1990: An analysis on the environment of squall line in Taiwan area. *Atmospheric Sciences 18*, 149-158 (in Chinese).

Durran, D.R. and *Klemp, J.B.*, 1982: The effects of moisture on trapped mountain lee waves. *J. Atmos. Sci. 39*, 2490-2506.

EPA (Environment Protection Administration of the Republic of China), 1991: The Annual Assessment Report of the Air Pollution Control in Taiwan area for 1991 (in Chinese).

Fovell, R.G. and *Ogura, Y.*, 1988: Numerical simulation of a midlatitude squall line in two dimensions. *J. Atmos. Sci. 45*, 3846-3879.

Galloway, J.N., Likens, G.E., Keene, W.C. and *Miller, J.M.*, 1982:The composition of precipitation in remote areas of the world. *J. Geophy. Res. 87*, 8771-8786.

Hegg, D.A., Rutledge, S.A. and *Hobbs, P.V.*, 1984: A numerical model for sulfur chemistry in warm-frontal rainbands. *J. Geophy. Res. 89*, No. D5, 7133-7147.

Klemp, J.B. and *Wihelmson, R.B.*, 1978: The simulation of three-dimensional convective storm dynamics. *J. Atmos. Sci. 35*, 1070-1096.

Kuo, Y.H. and *Chen, G.T.J.*, 1990: The Taiwan area mesoscale experiment (TAMEX): An overview. *Bull. Amer. Meteor. Soc. 71*, 488-503.

Likens, G.E. and *Bormann, F.H.*, 1974: Acid rain: A serious regional environmental problem. *Sciences 184*, 1176-1179.

Lin, Y.-J., Chen Wang, T.-C., Pusken, R.W., Shen, H. and *Deng, Z.-S.*, 1990: Characteristics of a subtropical squall line determined from TAMEX dual-Doppler data. PART II: Dynamic and thermodynamic structures and momentum budget. *J. Atmos. Sci. 47*, 2382-2399.

Lu, S.-C., Chen, F.-L. and *Miu, T.-C.*, 1985: The effect of air pollution on the pH value of rainwater over Taiwan area. *Atmospheric Sciences 2*, 69-72 (in Chinese).

National Research Council, 1983: *Acid Deposition Atmospheric Processes in Eastern North America: A Review of Current Scientific Understanding*. National Academy Press.

Rutledge, S.A., Hegg, D.A. and *Hobbs, P.V.*, 1986: A Numerial model for sulfur and nitrogen scavenging in narrow cold-front rainbands. 1. Model description and discussion of microphysical fields. *J. Geophy. Res. 91*, No. D13, 14385-14402.

Sun, Y.-C. and *Wu, R.-Y.*, 1980: The acid rain in the Taiwan area. *Scientific Development 8*, 428-434. Published by National Science Council, Rep. of China (in Chinese).

Wang, C.T.-C., Lin, Y.-J., Pasken, R.W. and *Shen, H.*, 1990: Characteristics of a subtropical squall line determined from TAMEX dual-Doppler data. Part I: Kinematic structure. *J. Atmos. Sci. 47*, 2357-2381.

Zhao, D., Xiong, J., Xu, Y. and *Chan, W.H.*, 1988: Acid rain in southwestern China. *Atmospheric Environment 22*, 349-358.

Appendix
Dynamic equations for the model

The model equations are cast in terrain-following coordinates (x,ζ) with

$$\xi = \frac{Z_t(Z - Z_S)}{Z_t - Z_S}, \tag{1}$$

where $Z_s = Z_s(x)$ is the height of the terrain above $Z = 0$ and Z_t is the height of the top of the model. The three tensor transformation terms used to describe the equations in the (x, ζ) coordinate system are

$$H^* = G^{\frac{1}{2}} = \frac{\partial \xi}{\partial z} = \frac{Z_t}{Z_t - Z_S}. \tag{2a}$$

$$G^{13} = \frac{\partial \xi}{\partial x} \frac{(\xi - Z_t)}{(Z_t - Z_S)} \tag{2b}$$

Using the above expressions, the momentum equations can be written as

$$\frac{\partial u}{\partial t} + C_p \bar{\theta}_v \left[\frac{\partial \pi}{\partial x} + G^{13} \left(\frac{\partial \pi}{\partial \xi} \right) \right] = A\tilde{D}X + \tilde{D}_u K_m, \tag{3a}$$

$$\frac{\partial w}{\partial t} + C_p \bar{\theta}_v \left[H^* \left(\frac{\partial \pi}{\partial \xi} \right) \right] = A\tilde{D}Z + q \left[\frac{\theta}{\bar{\theta}} - 1 + 0.64 \, (q_v - \overline{q_v}) \right] + \tilde{D}_w K_m, \quad (3b)$$

where

$$\theta_v = \theta (1 + 0.61 \, q_v), \quad (4a)$$

$$A\tilde{D}X = -u \left[\frac{\partial u}{\partial x} + G^{13} \left(\frac{\partial u}{\partial \xi} \right) \right] + wH^* \left(\frac{\partial u}{\partial \xi} \right), \quad (4b)$$

$$A\tilde{D}Z = -u \left[\frac{\partial w}{\partial x} + G^{13} \left(\frac{\partial w}{\partial \xi} \right) \right] + wH^* \left(\frac{\partial w}{\partial \xi} \right), \quad (4c)$$

$$\begin{aligned} \tilde{D}_u = {} & \frac{\partial}{\partial x} \left[2 \left(\frac{\partial u}{\partial x} + G^{13} \left(\frac{\partial u}{\partial \xi} \right) \right) - \frac{2}{3} \left(\frac{\partial u}{\partial x} + G^{13} \frac{\partial u}{\partial \xi} + H^* \frac{\partial w}{\partial \xi} \right) \right] \\ & + G^{13} \frac{\partial}{\partial x} \left[2 \left(\frac{\partial u}{\partial x} + G^{13} \left(\frac{\partial u}{\partial \xi} \right) \right) - \frac{2}{3} \left(\frac{\partial u}{\partial x} + G^{13} \frac{\partial u}{\partial \xi} + H^* \frac{\partial w}{\partial \xi} \right) \right] \\ & + H^* \frac{\partial}{\partial \xi} \left(H^* \frac{\partial u}{\partial \xi} + \frac{\partial w}{\partial} x + G^{13} \frac{\partial w}{\partial \xi} \right), \end{aligned} \quad (5a)$$

$$\begin{aligned} \tilde{D}_w = {} & \frac{\partial}{\partial x} \left(H^* \frac{\partial u}{\partial \xi} + \frac{\partial w}{\partial x} + G^{13} \frac{\partial w}{\partial \xi} \right) + G^{13} \frac{\partial}{\partial \xi} \left(H^* \frac{\partial u}{\partial \xi} + \frac{\partial w}{\partial x} + G^{13} \frac{\partial w}{\partial \xi} \right) \\ & + H^* \frac{\partial}{\partial \xi} \left[2 H^* \frac{\partial w}{\partial \xi} - \frac{2}{3} \left(\frac{\partial u}{\partial x} + G^{13} \frac{\partial u}{\partial \xi} + H^* \frac{\partial w}{\partial \xi} \right) \right], \end{aligned} \quad (5b)$$

θ is the potential temperature, q_v, q_c, and q_r are the mixing ratio of water vapor, cloud water and rain water, respectively, and θ_v is the virtual potential temperature. Bars over individual variables refer to the initial undisturbed state.

In Eqs. (3a) and (3b) the eddy mixing coefficient K_m is estimated according to *Lilly* (1962). The first law of thermodynamics is taken to be

$$\begin{aligned} \frac{\partial \theta}{\partial t} = {} & - \left[\left(u \frac{\partial \theta}{\partial x} + u G^{13} \frac{\partial \theta}{\partial \xi} \right) + H^* \left(w \frac{\partial \theta}{\partial \xi} \right) \right] + \left(\frac{\partial}{\partial x} + G^{13} \frac{\partial}{\partial \xi} \right) \left[K_h \left(\frac{\partial \theta}{\partial \xi} + G^{13} \frac{\partial \theta}{\partial \xi} \right) \right] \\ & + H^* K_h \left(\frac{\partial}{\partial z} \frac{\partial \theta}{\partial \xi} \right), \end{aligned} \quad (6)$$

where K_h is the eddy diffusivity of heat. The value of K_h is assumed to be three times of K_m in this study. The pressure equation model takes the form

$$\frac{\partial \Pi}{\partial t} + \frac{\overline{C}^2}{C_p \overline{\theta}_v}\left[\frac{\partial u}{\partial x} + G^{13}\left(\frac{\partial u}{\partial \xi}\right) + \frac{H}{\overline{\rho}}\frac{\overline{\partial \rho w}}{\partial \xi}\right] = 0 \tag{7}$$

and Exner function Π is the non-dimensional pressure in the form $\left(\frac{P}{P_0}\right)^{\frac{R_d}{C_p}}$. Here P_0 is the base state pressure at ground level and R_d is the gas constant for dry air. C is the speed of sound.

The mixing ratio of water vapor, q_v, mixing ratio of cloud water, q_c, and the mixing ratio of rain water, q_r, are considered in the model. The equations for q_v, q_c, q_r are

$$\frac{\partial q_v}{\partial t} = -\left[\left(u\frac{\partial q_v}{\partial x} + uG^{13}\frac{\partial q_v}{\partial \xi}\right) + H^*\left(w\frac{\partial q_v}{\partial \xi}\right)\right] + \left(\frac{\partial}{\partial x} + G^{13}\frac{\partial}{\partial \xi}\right)\left[K_h\left(\frac{\partial q_v}{\partial x} + G^{13}\frac{\partial q_v}{\partial \xi}\right)\right.$$

$$\left. + H^*\frac{\partial}{\partial \xi}\left(K_h H\frac{\partial q_v}{\partial \xi}\right)\right], \tag{8}$$

$$\frac{\partial q_c}{\partial t} = -\left[\left(u\frac{\partial q_c}{\partial x} + uG^{13}\frac{\partial q_c}{\partial \xi}\right) + H^*\left(w\frac{\partial q_c}{\partial \xi}\right)\right] + \left(\frac{\partial}{\partial x} + G^{13}\frac{\partial}{\partial \xi}\right)\left[K_h\left(\frac{\partial q_c}{\partial x} + G^{13}\frac{\partial q_c}{\partial \xi}\right)\right]$$

$$+ H^*\frac{\partial}{\partial \xi}\left(K_h H\frac{\partial q_c}{\partial \xi}\right), \tag{9}$$

$$\frac{\partial q_r}{\partial t} = -\left[\left(u\frac{\partial q_r}{\partial x} + uG^{13}\frac{\partial q_r}{\partial \xi}\right) + H^*\left(w\frac{\partial q_r}{\partial \xi}\right)\right] + \left(\frac{\partial}{\partial x} + G^{13}\frac{\partial}{\partial \xi}\right)\left[K_h\left(\frac{\partial q_r}{\partial x} + G^{13}\frac{\partial q_r}{\partial \xi}\right)\right]$$

$$+ H^*\frac{\partial}{\partial \xi}\left(K_h H\frac{\partial q_r}{\partial \xi}\right). \tag{10}$$

IDŐJÁRÁS

Quarterly Journal of the Hungarian Meteorological Service
Vol. 101, No. 3, July–September 1997, pp. 199–213

A case study on generation, conversion and dissipation of kinetic energy during the Bay of Bengal depression of 4-8 July 1979

R. K. Singh[1] and **U. S. Singh**[2]

[1]*Agrometeorology Section,*
G.B. Pant University of Agriculture and Technology, Hill Campus,
Ranichauri-249 199, Tehri-Garhwal, India

[2]*Department of Geophysics, Banaras Hindu University,*
Varanasi-221005, India

(Manuscript received 8 February 1995; in final form 19 July 1996)

Abstract—The vertical motion was obtained through the solution of the omega equation at 200, 400, 600 and 800 hPa surfaces over the Indian region for a depression over the head of the Bay of Bengal using MONEX-1979 data at 1.875 deg. lat/long grid resolution. Using velocity components as input, generation, conversion and dissipation of zonal and eddy kinetic energy have been computed at different isobaric surfaces. The zonal kinetic energy shows decreasing trend with altitude, with a minimum at 400 hPa and a maximum at 200 hPa which may be associated with the jet stream. The downward transfer of eddy kinetic energy from the upper to the middle troposphere seems to be a vital source of kinetic energy in the middle troposphere. Effects of the depression were observed to increase the eddy kinetic energy in the lower troposphere. The dissipation of kinetic energy throughout the atmosphere with a minimum at about the 400 hPa surface has been observed.

Key-words: kinetic energy, synoptic feature, monsoon depression.

1. Introduction

The southwest monsoon is generated due to the uneven heating of land and ocean during the summer. Usually 5 to 8 disturbances develop over the Bay of Bengal and the Arabian Sea at a frequency of 2 to 3 per month during the SW monsoon. Lows, depressions or deep depressions all are cyclones with moderate winds, they only differ in their wind intensity within the distance of 250 km from the center. Depressions follow northerly or northwesterly paths and play a very important role in bringing copious rain along its track over the Indian region. They are often associated with synoptic features of horizontal

convergence and upward vertical motion in the lower troposphere followed by horizontal divergence in the upper troposphere near to and in advance of the depression center. At the rear of the center, the horizontal divergence and the vertical motion become reversed. Movement and deviation of the depression mainly depend upon the generation, conversion and dissipation of zonal and eddy kinetic energy in the atmosphere. Hence, the study of generation, conversion and dissipation of kinetic energy during the depression period is of vital importance over the Indian region. In the past, several investigations have been made on the energy budget of the atmosphere over the Indian region including *Rao* and *Rajamani* (1968), *Keshavamurty* and *Awade* (1970), *Rao* and *Rajamani* (1970, 1972), *Rao et al.* (1978), *Singh et al.* (1980), *Desai* (1986), *Rajamani* and *Kulkarni* (1986) and *Masters* and *Kung* (1986). *Anjaneyulu* (1971) estimated the kinetic energy over the Indian monsoon trough zone and found that the Indian monsoon trough zone is an exporter of kinetic energy in the upper troposphere. *Mandal et al.* (1981) studied the kinetic energy budget of a cyclone over the Arabian Sea in June 1979. *Saha* and *Saha* (1988) discussed the thermal budget of this depression.

In this paper, an attempt has been made to study the generation, conversion and dissipation of zonal and eddy kinetic energy at different isobaric surfaces in the atmosphere to present the analysis of the energetics of a depression of 4–8 July formed over the Bay of Bengal during MONEX 1979, at a grid resolution of 1.875° lat/long which has never been attempted in the past over the Indian region.

2. Weather and associated synoptic feature

Out of the several charts for contour analyses of the observed height and wind fields from the 100 hPa through the 1000 hPa surfaces, it has been considered adequate to present the charts for the observed contour heights (*Fig. 1*) at 100 hPa, 500 hPa, and 900 hPa surfaces on the 5 to 8 July 1979 at 12.00 UTC only for better understanding, because these charts are helpful to illustrate the position of the low and its trend during the occurrence of the disturbance. It has been observed that a region of low pressure with associated cyclonic circulation extending to the middle troposphere entered the northeastern part of the Bay across the Arakan Coast on 4 July. It was stationary without appreciable development until the 6 July, and then concentrated into a depression in the morning on 7 July with its center at 03.00 UTC near to 19.5°N, 89.5°E about 400 km east-southeast of Paradip (20°N, 87°E). Moving westwards it crossed the northern part of the Orissa Coast near Paradip in the afternoon of 8 July. The track of monsoon depression are shown in *Fig. 2*. Moving west-northwestwards, the depression weakened into a low over northwest Madhya Pradesh by the 10 July and merged with seasonal trough on 11 July. The

system was probably a deep depression till the morning of 8 July. Upper N/NE winds of 30–40 kt up to 0.9 km above sea level was reported on 8 July in the morning at Bhubaneswar. From the dropsonde reports of the research aircrafts of MONEX, which flew over the depression field on 7 July, it is seen that the depression sloped southwestwards by about 3 degrees of latitude between the surface and 500 hPa. The monsoon was generally weak over Assam and its adjacent states and over West Bengal during the week. It was active to vigorous over Orissa on 7 and 8 July and in Madhya Pradesh on 8 and 9. Moderate heat wave conditions prevailed over many parts of Uttar Pradesh and Bihar on 7 and 8 July.

The interesting point about this sequence of events was (a) an initial northward movement followed by (b) a rapid westward movement of the depression. There was a considerable difference in the position of the cyclonic velocity maximum on 4 July between 700 and 900 hPa. But later, this tended to even up.

3. Data and area of computation

As part of the FGGE level-IIIb data base, special grid point data sets for 12.00 UTC at 1.875 deg. lat/long grid resolution were obtained from the European Centre for Medium Range Weather Forecasts (ECMWF) for the Indian region at 100 hPa, 300 hPa, 500 hPa, 700 hPa, 850 hPa and 1000 hPa surfaces for the period 4–8 July 1979. The area of computation extends from 9.4 to 30°N and 69.4 to 101.3°E. There are 18 grid points in the zonal direction and 12 grid points in the meridional direction.

A cubic interpolation technique was applied to interpolate the grid point data to the 900 hPa surface using the wind data for the 100 hPa, 300 hPa, 500 hPa, 700 hPa, 850 hPa and 1000 hPa surfaces, thus resulting in input fields at the 100 hPa, 300 hPa, 500 hPa, 700 hPa and 900 hPa surfaces, which were used to compute the vertical velocity at the 200 hPa, 400 hPa, 600 hPa and 800 hPa surfaces, respectively.

4. Method of computation

The ECMWF analyses of u, v fields have been used to solve the nonlinear reverse balance equation (*Singh* and *Singh*, 1990) including the Jacobian and beta terms for the calculation of the geopotential and solenoidal wind fields U_ψ and V_ψ at the 100 hPa, 300 hPa, 500 hPa, 700 hPa and 900 hPa surfaces. These were considered as input fields for solving the omega equation at the 200 hPa, 400 hPa, 600 hPa and 800 hPa surfaces (*Singh* and *Singh*, 1992a).

The basic equations were used in deriving the formulae for various forms of energy and their transformation based on *Lorenz*'s (1955) formulation. The rate of change of zonal and eddy kinetic energy may be expressed as

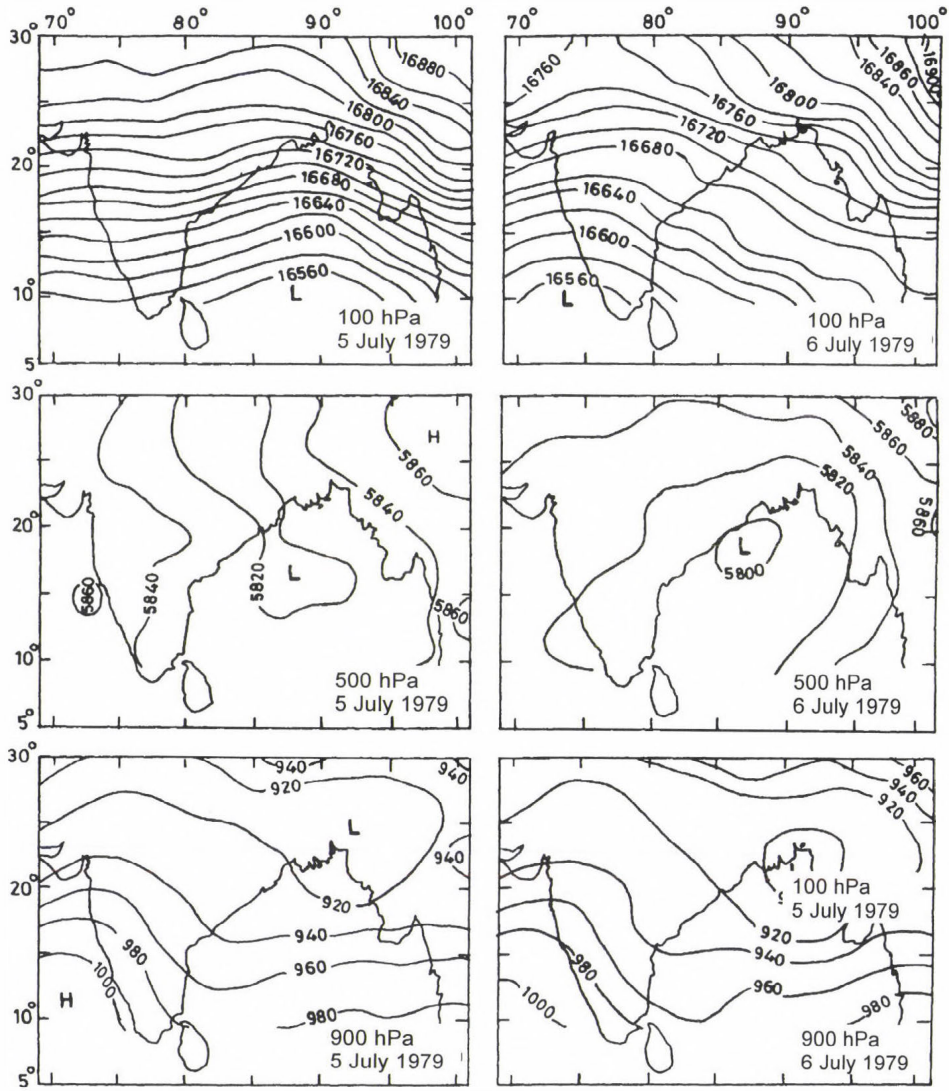

Fig. 1a. Observed contours in GPM at different isobaric surfaces on 5 and 6 July, 1979 (12.00 UTC).

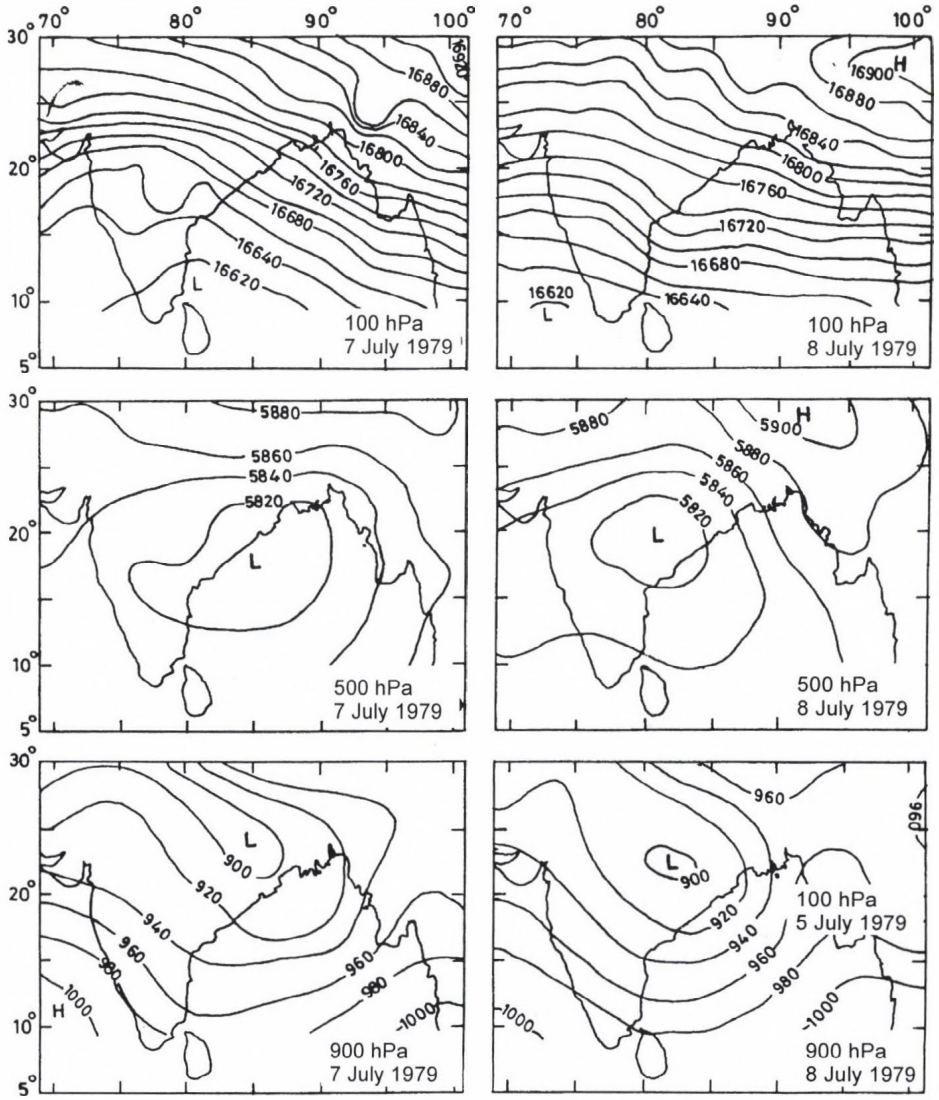

Fig. 1b. Observed contours in GPM at different isobaric surfaces on 7 and 8 July, 1979 (12.00 UTC).

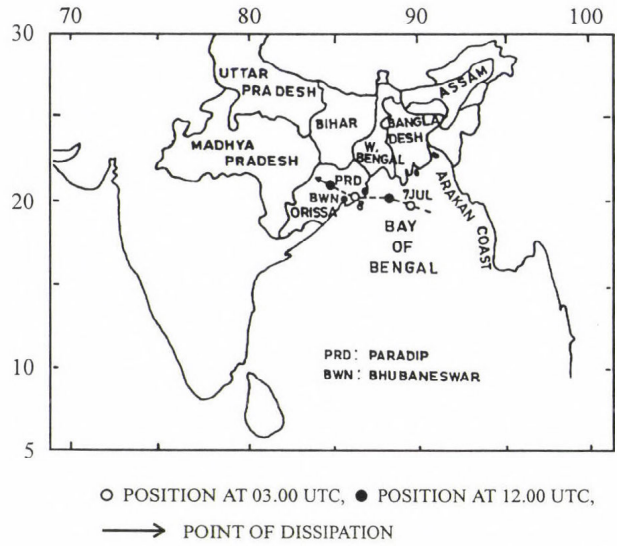

Fig. 2. Track of the Bay of Bengal depression of 4–8 July 1979.

$$\frac{\delta K_Z}{\delta t} = C_Z - C_k - D_Z, \tag{1}$$

$$\frac{\delta K_E}{\delta t} = C_E + C_K - D_E. \tag{2}$$

The various energy terms are defined as:

$$K_Z = \frac{1}{2} \int_M ([U]^2 + [V]^2)\, dM, \tag{3}$$

$$K_E = \frac{1}{2} \int_M ([U^{*2}] + [V^{*2}])\, dM, \tag{4}$$

$$C_Z = - \int_M [\omega]'' [\alpha]''\, dM, \tag{5}$$

$$C_E = \int_M [\omega^* \alpha^*]\, dM, \tag{6}$$

$$C_K = -\int_M [U^* V^*] \cos\phi \frac{\delta}{a\delta\phi}([U]\cos^{-1}\phi)\,dM - \int_M [V^{*2}]\frac{\delta[V]}{a\delta\phi}\,dM$$

$$+ \int_M [U^{*2}][V]\frac{\tan\phi}{a}\,dM - \int_M [U^*\omega^*]\frac{\delta}{\delta P}[U]\,dM - \int_M [U^*\omega^*]\frac{\delta}{\delta P}[V]\,dM, \quad (7)$$

$$D_Z = \int_M ([U][F_\lambda] + [V][F_\phi])\,dM, \quad (8)$$

$$D_E = \int_M ([U^* F_\lambda^*] + [V^* F_\phi^*])\,dM. \quad (9)$$

where F_ϕ and F_λ are the longitudinal and latitudinal components of the frictional force expressed as (*Oliger et al.*, 1970)

$$F_\lambda = \frac{\delta T_\lambda}{\delta Z} + F_{\lambda H}, \qquad F_\phi = \frac{\delta T_\phi}{\delta Z} + F_{\phi H}, \quad (10)$$

where T_λ and T_ϕ are the longitudinal and latitudinal components of the Reynold's stress. They are expressed as

$$T_\lambda = \rho K_{MV}\frac{\delta U}{\delta Z}, \qquad T_\phi = \rho K_{MV}\frac{\delta V}{\delta Z}, \quad (11)$$

where K_{MV} is the vertical kinematic eddy viscosity. The formulation of the horizontal eddy viscosity terms $F_{\lambda H}$ and $F_{\phi H}$ was obtained from *Smagorinsky* (1963).

Energy integrals are denoted as follows:

$$[X] = \frac{1}{(\lambda_1 - \lambda_2)}\int_{\lambda_1}^{\lambda_2} X\,d\lambda \qquad : \text{zonal mean},$$

$$\bar{X} = \frac{1}{A}\int_{\lambda_1}^{\lambda_2}\int_{\phi_1}^{\phi_2} X\,d\lambda\,d\phi \qquad : \text{areal mean},$$

$$X = [X] + X^* = X'' + \bar{X},$$

$$[X]'' = [X] - \bar{X},$$

where A is the area considered, X is any arbitrary function, [ ] represents the zonal mean, (-) the areal mean, * represents the deviation from the zonal mean, and [ ]" the perturbation in the zonal mean field upon its areal mean.

5. *Advection of energy terms*

Since we have performed the computations over a limited region it is necessary, as pointed out by *Smith* (1969), to compute the advection of energy terms. *Rao* and *Rajamani* (1972) and *Pandey et al.* (1989) computed the fluxes at the boundary and noted that even for a depression, the horizontal advection of available potential energy and kinetic energy may be safely neglected. We have also computed the fluxes at the boundary which were observed to be insignificant.

6. *Discussion of results*

Fig. 3 shows the vertical distribution of zonal (K_Z) and eddy (K_E) kinetic energy on 5, 6 and 7 July 1979, 12.00 UTC at the 200 hPa, 400 hPa, 600 hPa and 800 hPa surfaces, respectively. The vertical profile for the zonal kinetic energy indicates that it decreases from the 800 hPa to the 400 hPa surface where it becomes minimum. The westerlies of the lower troposphere weaken with height and changes to easterlies above 400 hPa (usually in the mid troposphere) where the winds and as such the kinetic energy have minimum values. Above 400 hPa the kinetic energy increases gradually up to the 200 hPa surface. In general, the zonal kinetic energy is larger than the eddy kinetic energy at each level in the vertical with a minimum at about 400 hPa. *Kida* (1977), *Pagnotti* and *Bosart* (1984), *Rajamani* and *Kulkarni* (1986) noted that the zonal kinetic energy is larger than the eddy kinetic energy. The sharp increase of the zonal kinetic energy above 400 hPa is due to the combined effects of sub-tropical westerly and tropical easterly jets. The eddy kinetic energy above 400 hPa is smaller than the zonal kinetic energy as the perturbations in the upper troposphere are extremely small. In the lower and middle troposphere we noted a gradual decrease in the zonal as well as in the eddy kinetic energy from 800 hPa to 400 hPa. This is because of the gradual decrease in the south-westerly current (monsoon current) along with the embedded depression in the lower troposphere/on the surface. *Kung* (1966) found maximum generation of kinetic energy by pressure forces to be strongest near the jet stream level. A secondary maximum exists in the planetary boundary layer, where larger temperature contrasts and strong ageostrophic components of motion are found. As the westerly decreases with height and becomes easterly around an anticyclonic circulation situated in the upper troposphere over the Indian peninsula during the period of the study, the lowest value of the zonal kinetic energy seems to occur due to this reason. The eddy kinetic energy distribution in the lower troposphere showed a marginal increase from 5 to 7 July as the depression intensified on 7 July.

Fig. 4 shows the vertical distribution of the zonal (C_Z) and the eddy (C_E) conversion of available potential energy to kinetic energy on 5, 6 and 7 July 1979, 12.00 UTC at the 200 hPa, 400 hPa, 600 hPa and 800 hPa surfaces,

respectively. We note that there was a conversion from zonal available potential energy to zonal kinetic energy above 400 hPa on 5 July and a conversion from zonal kinetic energy to zonal available potential energy below 400 hPa. This changed on 5 and 7 July from A_Z to K_Z below 400 hPa and K_Z to A_Z above 400 hPa. Thus, during the active phase of the depression, the conversion was from K_Z to A_Z on 5 July, then it was changed and the energy was converted from A_Z to K_Z on 6 and 7 July in the lower and middle troposphere. Thus, the effects of the depression on the active days (6th and 7th) were noted to introduce a conversion of energy from $K_E \rightarrow A_E \rightarrow A_Z \rightarrow K_Z$ in the lower and middle troposphere.

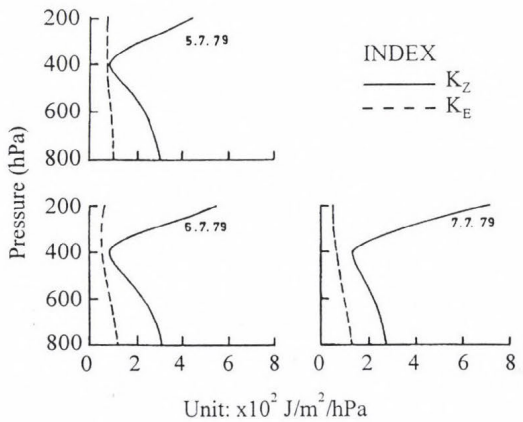

Fig. 3. Vertical distribution of zonal and eddy kinetic energy from 5 to 7 July 1979 (12.00 UTC).

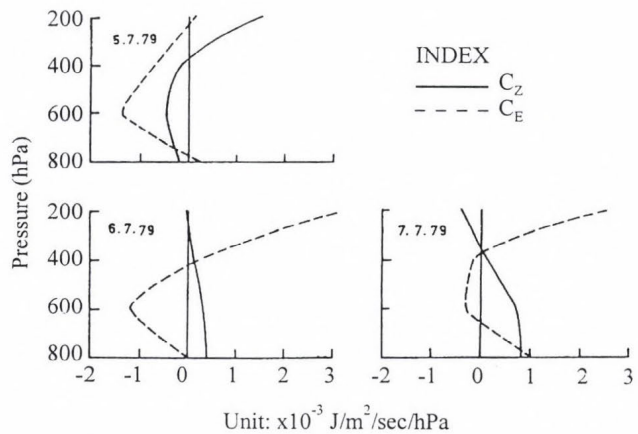

Fig. 4. Vertical distribution of C_Z and C_E from 5 to 7 July 1979 (12.00 UTC).

The conversion from eddy kinetic energy to eddy available potential energy on 5 July had a maximum at 600 hPa and from 800 to 200 hPa the eddy kinetic energy was acting as a source of eddy available potential energy. On the following days, i.e. on 6 and 7 July, the region of negative conversion in the middle troposphere was decreased above 400 hPa and below 600 hPa it changed to a positive value indicating that the eddy kinetic energy drew its energy from the eddy available potential energy as the depression became active on 7 July.

In the middle troposphere there was a conversion of eddy available potential energy to zonal available potential energy (*Singh* and *Singh*, 1992b; Fig. 4 a-c). This loss of eddy available potential energy was maintained by the eddy kinetic energy which was acting as a source for its conversion from eddy kinetic energy to eddy available potential energy around 600 hPa. Thus, in the middle troposphere we note that the mean flow drew its potential energy from A_E, and A_E drew its energy from K_E. *Kung* (1966) noted that there must be a downward transfer of kinetic energy from the upper to the middle troposphere. Through this result it seems there must have been a transfer of eddy kinetic energy from the lower as well as the upper troposphere to the mid-troposphere.

Fig. 5 shows the vertical distribution of each component of C_K, namely C_{K1} through C_{K5}, along with the sum of these components on 5, 6 and 7 July 1979, 12.00 UTC at the 200 hPa, 400 hPa, 600 hPa and 800 hPa surfaces, respectively. It was observed that the contribution of C_{K3} was insignificant at each level in the vertical during the life cycle of the depression. Positive values of the conversion from zonal to eddy kinetic energy in C_{K1} were observed in the layer between 450 hPa and 200 hPa on 5 July which indicated that the transfer of momentum due to eddies happened along the gradient of the meridional wind whereas below 450 hPa it was against the gradient with a peak at 600 hPa extending up to the 750 hPa surface. The horizontal transfer of momentum was gradually penetrating downward in the middle and upper troposphere along the gradient of the meridional wind on 6 and 7 July with the depth of penetration up to 700 hPa on 7 July with a maximum around 400 hPa. *Masters* and *Kung* (1986) observed large generation of K_E due to a cross isobaric flow in the upper troposphere. The contribution of C_{K2} was also significant and mostly negative from 5 to 7 July, except on the 7th between 350 hPa and 600 hPa, where it showed a positive value, indicating that, in general, the meridional transfer of mean meridional momentum was against the gradient of meridional wind throughout the atmosphere, except on the active phase of the depression what was observed on 7 July in the middle troposphere. The contribution of C_{K4} illustrates the vertical transfer of zonal momentum which was mostly upward between 800 hPa and 200 hPa with minima in the middle troposphere showing a downward transfer on the 7 July around 600 hPa. This seemed to be due to the strong sinking motion at 600 hPa on 7 July between 90°E to 100°E longitude and 10°N to 30°N latitude (*Singh* and *Singh*, 1992a).

The contribution of C_{K5} is dependent upon the vertical transfer of the mean meridional momentum which shows that on 5 July it was throughout upward with a maximum at 600 hPa, which continued on 6 July with a change over to upward in the lower and upper troposphere. On 7 July it was dominated by an upward transfer of the mean meridional momentum from 800 hPa to 400 hPa. The combined effects of the transfer of momentum showed that on 5 July, between 800 hPa and 400 hPa, the meridional transfer of momentum due to eddies was against the gradient of the meridional wind. The eddy kinetic energy acted as a source of zonal kinetic energy below 400 hPa resulting in a barotropically stable atmosphere. This continued on 6 July also, whereas on 7 July from 800 hPa to 600 hPa the eddy kinetic energy was acting as a source of zonal kinetic energy indicating that this atmospheric layer was barotropically stable, while between 650 hPa and 200 hPa the zonal kinetic energy was acting as a source of eddy kinetic energy resulting in barotropic instability in the middle and upper troposphere. Thus, we conclude that in the lower and middle troposphere which was barotropically stable, the eddy kinetic energy was acting as a source of K_Z, whereas in the upper troposphere above 400 hPa, where K_Z acted as a source of K_E, barotropically unstable conditions prevailed gradually strengthening the barotropic instability in the middle and upper troposphere. Besides that, the effects of the depression were observed to increase the conversion from K_E to K_Z from 5 to 7 July in the lower troposphere. *Masters* and *Kung* (1986) also noted that the upper troposphere acts as an important energy source by the significant downward transport of kinetic energy to mid-troposphere.

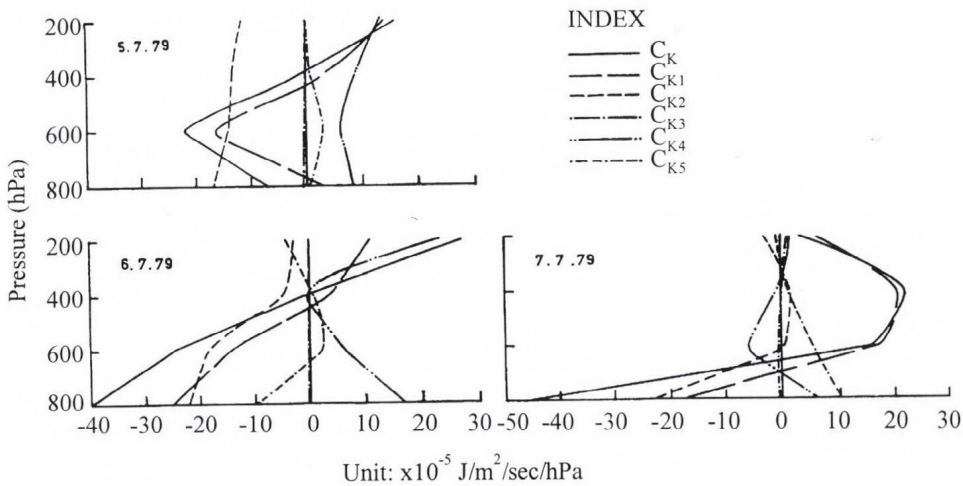

Fig. 5. Vertical distribution of C_K with its components from 5 to 7 July 1979 (12.00 UTC).

Fig. 6 shows the vertical distribution of zonal (D_Z) and eddy (D_E) dissipation of the kinetic energy on 5, 6 and 7 July 1979, 12.00 UTC at the 200 hPa, 400 hPa, 600 hPa and 800 hPa surfaces, respectively. It can be seen that the maximum dissipation of the eddy kinetic energy is at 800 hPa on 5 July with a gradual decrease in its magnitude up to 400 hPa, which further shows gradual increase in zonal and eddy dissipation of kinetic energy in the upper troposphere. Each day we observed a larger eddy dissipation as compared to the zonal dissipation in the lower and middle troposphere, whereas in the upper troposphere the zonal dissipation of kinetic energy exceeded the eddy dissipation of kinetic energy during the active phase of the depression, i.e. 7 July. In the lower troposphere, the larger number of eddies as well as the zonal dissipation of kinetic energy seemed to be due to the vertical diffusion of the momentum, whereas in the upper troposphere the horizontal diffusion was responsible for the gradual increase in the zonal and eddy dissipation of the kinetic energy.

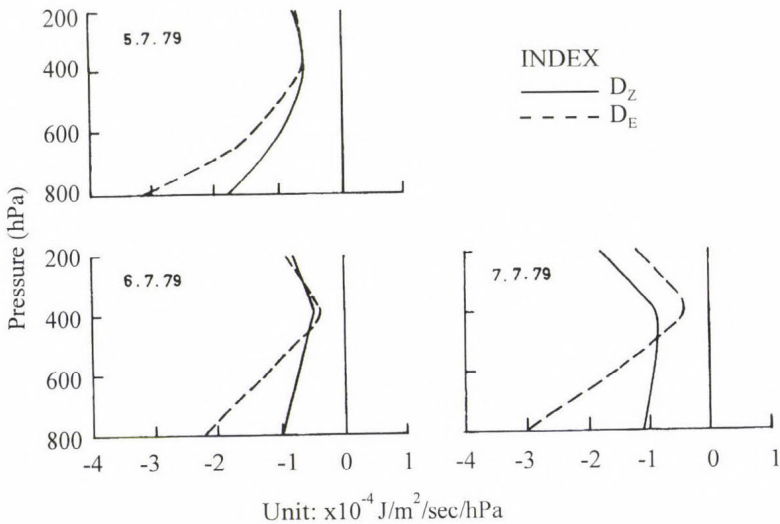

Fig. 6. Vertical distribution of D_Z and D_E from 5 to 7 July 1979 (12.00 UTC).

7. Summary

From our study it may be concluded that:

(1) The zonal kinetic energy decreases with height in the vertical during the life cycle of the depression, resulting in a minimum at 400 hPa. Then it increases with a maximum at 200 hPa, which seems to be associated with the jet stream. Above 400 hPa the eddy available potential energy

acts as a source of the eddy kinetic energy, whereas in the middle troposphere, the eddy kinetic energy is transferred to eddy available potential energy. Hence, the downward transfer of kinetic energy from upper to middle troposphere appears to be an important mechanism to supply the eddy kinetic energy in the middle troposphere. Besides that, a decrease in the loss of eddy kinetic energy or an increase in the gain of eddy kinetic energy results in the lower troposphere due to the effects of the depression as the conversion tends to become positive or reduce the magnitude of a negative C_E. This results in the zonal conversion from potential energy to kinetic energy associated with the meridional overturning, the warm air is associated with the rising motion and the cold air with the sinking motion.

(2) The depression generally introduces a conversion of eddy available potential energy to eddy kinetic energy, which results in an increase in the amount of conversion from A_E to K_E or in a change of the existing direction of conversion from K_E to A_E into A_E to K_E in the lower troposphere, whereas in the upper troposphere this positive conversion is due to effects of the anticyclonic circulation above 400 hPa, resulting in a strong subsidence and hence cooling. In the zonal form of energy conversion, the depression introduces a conversion from K_Z to A_Z during the active phase of the depression in the lower and middle troposphere.

(3) The zonal and eddy dissipation of kinetic energy takes place due to the frictional forces throughout the atmosphere. In the lower troposphere, larger dissipation of the zonal and eddy kinetic energy was noted which may be due to the vertical diffusion of momentum and the subgrid scale mixing. However, in the upper troposphere, the larger dissipation of kinetic energy must be due to the horizontal diffusion of momentum. The minimum dissipation of zonal as well as eddy kinetic energy was observed at the 400 hPa surface where zonal and eddy kinetic energy was being minimum.

(4) A gradual strengthening of barotropic instability in the middle and upper troposphere and a barotropic stability in the lower troposphere was observed during the life cycle of the depression.

Acknowledgements—The authors express their appreciation to *R. N. Maurya* for his help during the preparation of the manuscript, and to *Shri P. K. Chaterjee* for neatly typing the manuscript.

References

Anjaneyulu, T.S.S., 1971: Estimates of kinetic energy over the Indian monsoon trough zone. *Q. J. R. Meteor. Soc. 97*, 103-109.

Desai, D.S., 1986: Study of energetics of strong and break monsoon. *Mausam 37*, 365-367.

Keshavamurty, R.N. and *Awade, S.T.*, 1970: On the maintenance of the mean monsoon trough over North India. *Mon. Wea. Rev. 98*, 315-319.

Kida, H., 1977: A numerical investigation of the atmospheric general circulation and stratospheric-tropospheric mass exchange: I. Long term integration of a simplified general circulation model. *J. Meteor. Soc. Japan 55*, 52-70.

Kung, E.C., 1966: Kinetic energy generation and dissipation in the large scale atmospheric circulation. *Mon. Wea. Rev. 94*, 67-82.

Lorenz, E.N., 1955: Available potential energy and the maintenance of the general circulation. *Tellus 7*, 157-167.

Mandal, G.S., Rao, R.V.R.K. and *Gupta, S.C.*, 1981: Characteristics of an Arabian Sea cyclone. *Mausam 32*, 139-144.

Masters, S.E. and *Kung, E.C.*, 1986: An energetics analysis of cyclonic development in the Asian winter monsoon. *J. Meteor. Soc. Japan 64*, 35-51.

Oliger, J.E., Wellck, R.E., Kasahara, A. and *Washington, W.M.*, 1970: Description of NCAR global circulation model. *NCAR Technical Notes-56 + STR*. National Center for Atmospheric Research, Boulder, Colorado, 94.

Pagnotti, V. and *Bosart, L.*, 1984: Comparative diagnostic case study of east coast secondary cyclogenesis under weak versus strong synoptic scale forcing. *Mon. Wea. Rev. 112*, 5-30.

Pandey, S.N., Chattopadhyay, J. and *Singh, U.S.*, 1989: Studies of energy during strong and weak monsoon situations over India. *Mausam 40*, 417-420.

Rajamani, S. and *Kulkarni, J.R.*, 1986: On some energy aspects of the monsoon depression during its life cycle. *Mausam 37*, 9-16.

Rao, K.V. and *Rajamani, S.*, 1968: Diagnostic study of a monsoon depression by geostrophic baroclinic model. *Sci. Rep.* No. 54. India Met. Dep., 1-26.

Rao, K.V. and *Rajamani, S.*, 1970: Diagnostic study of a monsoon depression by geostrophic model. *Indian J. Meteor. Geophys. 21*, 187-194.

Rao, K.V. and *Rajamani, S.*, 1972: Study of heat sources and sinks and the generation of available potential energy in the Indian region during the southwest monsoon season. *Mon. Wea. Rev. 100*, 383-388.

Rao, K.V., Rao, G.S.P. and *Rajamani, S.*, 1978: Diagnostic study of a monsoon depression. *Indian J. Meteor. Geophys. 29*, 260-272.

Saha, K.R. and *Saha, S.*, 1988: Thermal budget of a monsoon depression in the Bay of Bengal during FGGE-MONEX-1979. *Mon. Wea. Rev. 116*, 342-354.

Singh, U.S. and *Singh, R.K.*, 1990: Solution of the balance equation over the Indian monsoon region. *Proc. Indian Nat. Sci. Acad. 56A*, 55-62.

Singh, U.S. and *Singh, R.K.*, 1992a: Vertical motion and diabatic heating over the Indian monsoon region during the Bay of Bengal depression of 5-8 July, 1979. *Pure Appl. Geophys. 138*, 115-133.

Singh, U.S. and *Singh, R.K.*, 1992b: Study of available potential energy of a depression pattern in the region of Bay of Bengal. *Időjárás 96*, 93-105.

Singh, S.S., Kulkarni, A.A. and *Bandyopadhyaya, A.*, 1980: The kinetic energy budget of monsoon circulation over the Indian region during ISMEX-1973. *Pure Appl. Geophys. 119*, 16-23.

Smagorinsky, J., 1963: General circulation experiments with the primitive equations: I. The basic experiment. *Mon. Wea. Rev. 91*, 99-164.

Smith, P.J., 1969: On the contribution of a limited region to the global energy budget. *Tellus 21*, 202-207.

List of symbols

a	—	radius of earth
C_K	—	transformation from zonal to eddy kinetic energy
C_Z , C_E	—	zonal and eddy conversion of available potential energy to kinetic energy
D_Z , D_E	—	zonal and eddy dissipation of kinetic energy
dM	—	mass increment
dP	—	pressure increment
dt	—	time increment
F_λ , F_ϕ	—	frictional forces per unit mass along the zonal and meridional direction.
K_Z , K_E	—	zonal and eddy kinetic energy
M	—	mass of the atmosphere
U, V	—	zonal and meridional component of wind
ω	—	vertical velocity
α	—	specific volume
λ, ϕ	—	longitude, latitide.

IDŐJÁRÁS

Quarterly Journal of the Hungarian Meteorological Service
Vol. 101, No. 3, July–September 1997, pp. 215–231

Solar radiation characteristics at Qena/Egypt

Sayed M. El-Shazly[1], **A. M. Abdelmageed** and **M. El-Noubi Adam**

Department of Physics, Faculty of Science,
South Valley University, Qena/Upper Egypt, E-mail: svalleyu@frcu.eun.eg

(Manuscript received 1 December 1995; in final form 24 June 1996)

Abstract—Measurements of the hourly global solar radiation (G) and its diffuse component (D) on a horizontal surface have been carried out in Qena/Upper Egypt in the period from June 1992 to May 1993. The corresponding diffuse fraction (D/G) is calculated. Diurnal variations of the results have been studied. Also the daily total values and their monthly and seasonal averages as well as their frequency distributions were computed and examined. The seasonal and climatic effects on the fluctuation of the results are discussed. These effects were particularly large during spring and winter months owing to the high fluctuation of the atmospheric conditions with respect to cloud amounts, water content, and concentration of aerosol dust particles. The influence of clouds has small effect on the results. The relative reduction of global solar radiation by cloud over the whole period is around 4.5% due to the low degree of cloudiness in the study region. The relation between the diffuse fraction and clearness index (G/G_0) shows that most of the points lie in the region of the high availability of the incoming solar radiation.

Key-words: global radiation, diffuse radiation, diffuse fraction, monthly and seasonal variations, effect of clouds, clearness index, radiation climate.

1. Introduction

Over the past years, a decided need for additional solar radiation data has arised due to the increased use of solar energy systems. The detailed knowledge of these data is of fundamental importance to the successful development of projects for the practical utilization of solar energy by agriculturists, hydrologists, architects and engineers, particularly in the region where sunshine is available in abundance (*Atwater* and *Ball*, 1981; *Moriarity*, 1991; *Kuye* and *Jagtap*, 1992; *Neuwirth*, 1980).

[1]Corresponding author

Qena is a city of abundant solar radiation along most of the months of the year. Accordingly, it would appear to be well suited to the use of solar energy in different application owing to the interest, which this form of clean energy presents to solve the energy demand problem. In this concern we attempt in this study to provide solar radiation information for designers of solar energy utilization systems under the climatic conditions of Qena/Egypt, which may also serve as a useful reference for system designers and users in other regions with similar climatic conditions.

2. General climate of Qena/Egypt

Qena is located in the south part of Egypt at latitude 26°10'N, longitude 32°43' E and elevation 78 m above sea level. Climatically, Qena lies within the subtropical region characterized by hot, dry and calm weather with low cloudiness (80% of the days of the year are cloudless) and nearly no precipitation. Trend values of average temperature and relative humidity range from 14.5°C in January to 34°C in July and from 21% in May and June to 48% in December, respectively. Significant percentage of winds is calm (52%). The prevailing winds are W, NW, SW and N, with percentages of occurrence of 15.9%, 11.83%, 11.7% and 4.52%, respectively. The majorority of winds range from 2 to 3.1 m s^{-1} and the least occurrence of speed intervals ranges from 8.8 to 10.8 m s^{-1}.

3. Experiments

Measurements of hourly global (G) and diffuse (D) solar radiation were made from sunrise to sunset from June 1992 to May 1993, using two Kipp and Zonen pyranometers (Model CM 6B). One of them is used to measure the global radiation and the other is fitted with a shadow band of radius of 610 mm and width of 60 mm, constructed following Kipp and Zonen rules, to measure the diffuse component. The pyranometer specifications meet the majority of the requirements set for class 1 radiation sensors by the World Meteorological Organization (*WMO*, 1983). The setting of the shadow band was checked twice a day making sure of the centering of the sun shade on the receiver head of the pyranometer all day around. Every few days the band position is adjusted according to the actual declination of the sun. Irradiances (G and D) in W m^{-2} were measured and integrated over 60 minutes period using a two-channel-integrator (Kipp and Zonen Model CC12). The instruments were used for the first time in this study and calibrated by the manufacturers themselves. The pyranometer has a directionality error <20 W m^{-2} at 100 W m^{-2} and a non linearity error $<1.5\%$, while the inaccuracy of the solar integrator lies within

0.2% + 1 digit. The measured values of D were multi-plied by a correction factor f (1 to 1.14), calculated daily to compensate the part of the diffuse sky radiation, which is obstructed by the shadow band. This value is determined by *Latimer* and *Mac Dowall*, 1971 as:

$$f = 1/(1 - F/D), \tag{1}$$

in which — assuming the isotropic distribution of sky radiance —

$$F/D = 2\omega / \pi r \cos^3 \delta \, (\sin\phi \, \sin\delta \, H_0 + \cos\phi \, \cos\delta \, \sin H_0), \tag{2}$$

where ω is the width of the band, r is its radius, δ is the solar declination, ϕ is the latitude of the station and H_0 is the hour angle of the sun at sunset.

The extinction by water vapor is given by *Iqbal* (1983):

$$a_W = 2.4959 \, U_1 \left[(1.0 + 79.034 \, U_1)^{0.6828} + 6.385 \, U_1\right]^{-1}, \tag{3}$$

where

$$U_1 = W m_r, \tag{4}$$

in which W is the perceptible water thickness in cm and m_r is the relative air mass. *Leckner* (1978) presented the following formula for calculating W:

$$W = 0.493 \, (\phi_r / T) \exp (26.23 - 5416/T), \tag{5}$$

where ϕ_r is the relative humidity in fraction of one and T is the ambient temperature in Kelvin.

The relative air mass m_r is given by *Kasten* (1966):

$$m_r = \left[\cos Z + 0.15 \, (93.885 - Z)^{-1.253}\right]^{-1}, \tag{6}$$

where Z is the zenith angle in degrees.

The extinction by aerosols is obtained from

$$a_A = 1 - T_A, \tag{7}$$

where T_A is the transmissivity after the extinction by aerosols:

$$T_A = \exp (-\tau_A m_r), \tag{8}$$

in which τ_A is the aerosol optical depth estimated with the aid of Rayleigh (T_R) and ozone (T_{oz}) transmissivities and water vapor absorption (a_W) (*Al-Jamal et al.*, 1987) as:

$$\tau_A = (-1/m_r) \ln [(I/I_0) / (T_{oz} \, T_R - a_W)], \tag{9}$$

I is the direct beam radiation (W m^{-2}) and I_0 is the corresponding extraterrestrial one (W m^{-2}) calculated using the following equations:

$$G = I \sin h + D, \tag{10}$$

where h is the solar elevation angle,

$$I_0 = 1367 \left(1 + 0.033 \cos(360 d_n/365)\right), \tag{11}$$

where d_n is the Julian day number.

4. Results and discussion

The different solar radiation components are functions of several variables (*Atwater* and *Ball*, 1981; *Kudish et al.*, 1983) such as the solar elevation angle, the nature and extent of cloudiness (cloud amount), the atmospheric scattering by air molecules (Rayleigh scattering), and aerosol (Mie scattering) as well as the absorption by atmospheric gases (H_2O, O_2, CO_2, O_3 in specific wavelength bands) and aerosol.

4.1 Characteristics of global solar radiation (G) on a horizontal surface

4.1.1 All sky conditions measurements (G_a)

(a) Hourly variation of global solar radiation (G_{ah})

Table 1 gives the average values of the hourly global solar radiation in Wh m^{-2} received on a horizontal surface through a day at different months in the measurement period (Local Apparent Time is used). From this table one can see clearly that the rise and fall of the hourly global solar radiation throughout the day is generally symmetrical with respect to the solar noon for all days the year around.

(b) Variation of daily totals of global solar radiation (G_{ad}).

Fig. 1 illustrates the variation of the daily totals of global solar radiation through the whole measurement period from June 1992 to May 1993. In this figure, the value of G_{ad} varies from 8713 Wh m^{-2} (at the day number 159: June 8) to 1564 Wh m^{-2} (at the day number 7: January 7) with remarkable variation from day to day. This "vibration" is due to the fluctuation of the atmospheric conditions with respect to water content, dust and amount and type of clouds, which change from hour to hour and day to day. According to the astronomical

Table 1. Results of mean values of hourly and daily global solar radiation (Wh m^{-2}) at all (G_a) and cloudless (G_c) sky conditions (June 1992–May 1993; Qena/Egypt)

LAT		Sr-5	5-6	6-7	7-8	8-9	9-10	10-11	11-12	12-13	13-14	14-15	15-16	16-17	17-18	18-SS	Daily totals
Jun 1992	G_a	2	86	282	514	718	882	997	1042	1018	928	776	578	351	136	11	8323
	G_c	2	87	285	518	720	885	1000	1043	1020	930	778	580	352	137	11	8358
Jul	G_a	1	79	279	503	704	868	983	103	101	926	766	564	343	1266	9	8210
	G_c	1	79	279	503	704	868	983	103	101	927	769	568	346	127	9	8220
Aug	G_a		45	229	455	662	820	952	100	978	880	719	511	281	79	3	7586
	G_c		45	229	455	664	821	954	100	981	878	718	510	279	79	3	7605
Sep	G_a		16	166	406	616	779	900	951	924	823	646	432	206	31		6873
	G_c		16	166	397	616	779	900	951	924	824	646	432	208	31		6896
Oct	G_a		2	89	301	508	686	801	843	819	712	544	330	122	6		5764
	G_c		2	90	303	509	687	804	846	825	720	554	335	123	6		5829
Nov	G_a			35	194	379	558	673	717	682	594	437	251	66	1		4588
	G_c			34	189	390	553	666	718	695	602	448	258	67	1		4662
Dec	G_a			9	124	306	458	574	651	627	558	431	258	79	3		4077
	G_c			9	119	301	467	589	655	650	578	438	257	73	3		4180
Jan 1993	G_a			1	58	233	414	556	647	665	627	497	348	163	27		4236
	G_c			0.8	61	248	445	596	690	719	682	574	402	197	32		4635
Feb	G_a			3	97	308	505	669	776	814	770	643	480	277	78	1	5419
	G_c			3	99	312	505	670	791	822	789	658	492	285	78	1	5635
Mar	G_a		1	25	179	400	613	784	884	914	859	740	556	331	112	4	6414
	G_c		1	27	194	415	632	795	890	924	872	736	539	317	107	4	6532
Apr	G_a		8	108	316	509	725	878	952	970	862	743	556	347	131	8	7111
	G_c		8	109	339	562	752	911	968	100	930	790	581	374	141	8	7561
May	G_a		32	200	428	618	774	904	987	974	832	708	539	327	186	11	7472
	G_c		33	203	438	639	792	955	1034	1046	977	826	625	384	153	12	8121
Summer	G_a	2	56	240	466	668	827	948	100	975	881	720	515	292	91	8	7670
	G_c	10	56	242	469	677	837	960	101	988	893	730	525	300	91	8	7824
Autumn	G_a		3	60	240	434	609	724	771	743	652	492	296	99	8		5110
	G_c		3	60	241	442	614	730	779	757	663	505	303	103	8		5324
Winter	G_a			5	90	286	471	622	725	746	698	573	413	215	52	2	4824
	G_c			5	92	295	490	650	751	788	753	620	452	243	54	2	5236
Spring	G_a	2	38	174	395	593	776	914	984	984	875	746	561	344	134	9	7551
	G_c	2	39	177	413	626	802	947	100	101	939	795	591	367	141	9	7976
Year	G_a	2	42	133	302	499	675	806	873	864	779	634	446	237	78	7	6289
	G_c	9	41	137	309	517	694	828	890	886	810	661	462	246	77	7	6590

cycle of the earth, the sites situated outside the tropics in the northern hemisphere have the maximum and minimum global solar radiation at the June solstice (June 20/21) and the December solstice (December 20/21), respectively (*Morris et al.*, 1982). The observed shift is due to the high amount of clouds observed at the June solstice (5 octas) in comparison to the clear sky in June 8, and the dense and dark clouds, which covered the sky from sunrise to sunset at January 7 (8 octas).

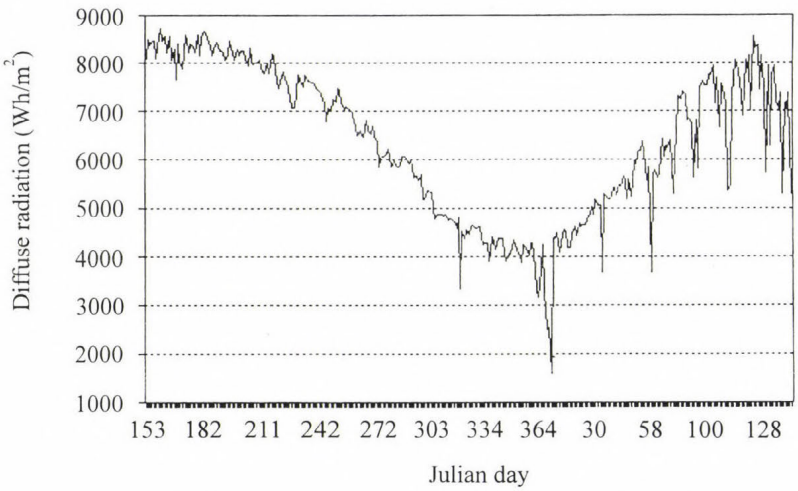

Fig. 1. Variation of daily totals of global solar radiation (June 1992–May 1993) in Qena/Egypt.

(i) Variation of monthly average of daily totals of global solar radiation (G_{ad})

The variation of the monthly average of G_{ad} are also included in Table 1. The average value of daily totals of G_{ad} ranges from 8323 Wh m^{-2} in June to 4077 Wh m^{-2} in December. The standard deviation has relatively high values at May $\pm$869), January ($\pm$829), and April ($\pm$749), compared with the small values at July ($\pm$194) and June ($\pm$246). This is due to the strong fluctuation of atmospheric dust particles and clouds in these three months (May, January, and April).

(ii) Variation of seasonal averages of G_{ad}

Table 1 gives the seasonal averages of G_{ad} as well as its average over the whole measurement period. From this table one can see that the average G_{ad} over the year is 6289 Wh m^{-2} with a seasonal variation from 4824 Wh m^{-2} in winter to 7670 Wh m^{-2} in summer. This relatively temperate variation is typical of the

climate of North Africa and also reflects the low degree of cloudiness in the study region (1 octa on the average through the measurement period). The standard deviation of the results, has high values in winter (±1023) and spring (±864) and a small value in summer (±529) indicates the higher stability of the atmosphere in the summer months.

(iii) Percentage frequency distribution of G_{ad}

The percentage frequency distributions of G_{ad} are given in *Table 2* for each month, season and the whole period, respectively. From this table, it can be seen that about 95.6% of the days in the year have values of G_{ad} within the range from 4–9 kWh m^{-2}. In summer 92.6% and in spring 80.6% of the measurements were observed in the range of 7–9 kWh m^{-2}, while in autumn 96.1% and in winter 86.5% were observed in the range of 4–7 kWh m^{-2}. In June, July and August, almost all days receive G_{ad} in the range of 7–9 kWh m^{-2} and 88.9% of these days get between 8 and 9 kWh m^{-2} in June and July. The above distribution of the solar radiation is characteristic for the climate of subtropical regions and indicates the richness of the study region in solar energy.

Table 2. Percentage of frequency distribution of daily totals of global solar radiation through the measurement period in Qena/Egypt

Range (kWh m^{-2})		1–2	2–3	3–4	4–5	5–6	6–7	7–8	8–9
June	1992	0.0	0.0	0.0	0.0	0.0	0.0	11.1	88.9
July		0.0	0.0	0.0	0.0	0.0	0.0	11.1	88.9
August		0.0	0.0	0.0	0.0	0.0	0.0	92.6	7.4
September		0.0	0.0	0.0	0.0	0.0	56.0	44.0	0.0
October		0.0	0.0	0.0	3.7	66.7	29.6	0.0	0.0
November		0.0	0.0	4.0	96.0	0.0	0.0	0.0	0.0
December		0.0	0.0	23.1	76.9	0.0	0.0	0.0	0.0
January	1993	3.8	7.7	3.8	76.9	7.7	0.0	0.0	0.0
February		0.0	0.0	7.7	0.0	76.9	15.4	0.0	0.0
March		0.0	0.0	0.0	0.0	31.3	43.8	25.0	0.0
April		0.0	0.0	0.0	0.0	14.8	22.2	59.3	3.7
May		0.0	0.0	0.0	0.0	10.5	5.3	52.6	31.6
Summer		0.0	0.0	0.0	0.0	0.0	7.4	49.4	43.2
Autumn		0.0	0.0	3.9	51.3	23.7	21.1	0.0	0.0
Winter		1.4	2.7	9.5	35.1	36.5	14.9	0.0	0.0
Spring		0.0	0.0	0.0	0.0	9.0	10.4	47.8	32.8
Year		0.3	0.7	3.4	21.8	17.1	13.4	24.2	19.1

4.1.2 Comparison between average global solar radiation (G_a) and global radiation at cloudless skies (G_c)

To illustrate the influence of clouds on the incoming global solar radiation, the behavior of global solar radiation in case of cloudless sky conditions (G_c) is discussed and compared with those measured in all sky conditions (G_a). The results of measurements of G_c are summarized in Table 1.

(a) Comparison between the hourly global solar radiation in all (G_{ah}) and cloudless (G_{ch}) sky conditions

According to Table 1, the comparison between the average values of G_{ch} and G_{ah} in the whole measurement period shows that:

(i) The course of G_{ch} is similar to that of G_{ah} with somewhat higher values of G_{ch}, because of the missing attenuation by clouds.

(ii) The average cloud effect seems to be small in Qena over the whole measurement period because the low effect in some months decreases the high one in other months. Also the study region is characterized by high thin clouds, which have only small effect in depleting the global solar radiation.

(b) Comparison between the daily totals of global solar radiation in all (G_{ad}) and cloudless (G_{cd}) sky conditions

As we already found in section (4.1.2.a) for (G_{ch}), the behavior of G_{cd} shows the same general pattern as G_{ad} for both monthly and seasonal averages, but with higher values. The relative percentage of exceeding G_{cd} by G_{ad} was found to be maximum in January (9%), May (8%) and winter (7.9%), while it is minimum in July (0.1%) and summer (2%). In the whole period the average value is (4.6%). This may be explained in terms of the elimination of cloud effect, which was maximum in January (1.79 octas), May (2.68 octas) and winter (1.61 octas) while it was minimum in July, September (0.08 octa) and summer (0.11 octa). As shown in Table 1 the average values of G_{cd} vary from 8358 Wh m^{-2} in June to 4180 Wh m^{-2} in December and from 7976 Wh m^{-2} in spring to 5236 Wh m^{-2} in winter with average value over the whole measurement period equals to 6590 Wh m^{-2}.

4.2 Characteristics of diffuse solar radiation (D)
4.2.1 All sky conditions measurements (D_a)

(a) Hourly variation of diffuse solar radiation (D_{ah})

Table 3 gives the results of hourly variation of diffuse solar radiation in Wh m^{-2} through the measurement period. The measured mean values of D_{ah} are maxi-

Table 3. Results of mean values of hourly and daily diffuse solar radiation (Wh m^{-2}) at all (D_a) and cloudless (D_c) sky conditions (June 1992–May 1993; Qena/Egypt)

LAT		Sr-5	5-6	6-7	7-8	8-9	9-10	10-11	11-12	12-13	13-14	14-15	15-16	16-17	17-18	18-SS	Daily totals
Jun 1992	D_a	2	56	126	172	202	219	227	237	235	224	206	183	147	83	10	2327
	D_c	2	56	123	168	197	213	219	230	229	219	201	178	145	82	10	2271
Jul	D_a	1	45	103	142	166	181	191	194	194	183	174	153	119	66	7	1920
	D_c	1	46	104	142	166	181	190	193	190	180	171	151	118	67	8	1908
Aug	D_a		28	96	141	154	170	178	180	181	172	166	138	103	44	2	1752
	D_c		26	96	141	148	163	171	173	171	163	152	135	100	42	2	1683
Sep	D_a		14	85	143	180	202	212	217	213	201	185	154	104	31		1943
	D_c		13	84	141	174	195	204	212	206	194	178	147	99	24		1871
Oct	D_a		2	49	105	133	160	168	173	167	161	141	111	61	5		1435
	D_c		2	50	104	134	157	164	168	162	155	136	108	60	5		1404
Nov	D_a			24	84	123	148	165	159	155	149	138	105	46			1297
	D_c			24	83	122	146	160	152	151	142	121	101	45	1		1247
Dec	D_a			7	58	104	133	141	154	150	137	119	99	49	2		1155
	D_c			8	58	104	125	133	142	128	120	104	91	45	2		1059
Jan 1993	D_a			1	38	88	129	150	160	172	170	142	118	74	17		1260
	D_c				35	78	110	130	135	143	136	124	104	71	21		1089
Feb	D_a			2	45	99	134	159	166	164	161	144	120	96	39	1	1330
	D_c			2	46	95	128	147	146	141	139	135	110	87	39	1	1216
Mar	D_a			17	83	139	168	190	199	207	203	196	179	133	62	3	1780
	D_c			19	91	150	180	197	198	206	200	186	169	132	68	4	1800
Apr	D_a		5	63	131	172	185	212	224	213	215	200	175	126	62	5	1988
	D_c		6	70	144	172	165	179	197	182	184	178	165	125	71	6	1843
May	D_a		27	108	139	176	265	280	281	275	245	231	187	133	73	10	2430
	D_c		27	118	148	166	184	201	220	229	206	197	155	116	73	8	2046
Summer	D_a	2	34	101	145	168	184	193	197	195	185	176	160	112	52	7	1899
	D_c	1	32	98	142	164	180	188	192	188	178	166	144	108	48	7	1838
Autumn	D_a		3	35	93	130	153	165	168	162	154	135	109	56	8		1371
	D_c		3	38	95	132	154	164	166	160	152	132	109	58	8		1371
Winter	D_a			4	48	103	141	102	170	179	174	155	128	89	29	2	1385
	D_c			4	45	93	124	143	148	145	141	132	110	82	32	1	1200
Spring	D_a	2	31	96	157	194	214	253	251	247	236	221	193	144	77	8	2323
	D_c	2	37	104	157	186	196	206	222	218	208	194	173	137	78	8	2126
Year	D_a	2	28	64	108	146	170	188	192	191	183	168	141	97	43	6	1726
	D_c	2	29	70	112	144	164	175	180	176	169	155	133	94	44	6	1652

mum in the hours around midday (11–13 LAT). Its average value over the whole measurement period is equal to 192 Wh m^{-2}, ranging from 237 Wh m^{-2} in June to 150 Wh m^{-2} in December. At early morning (Sunrise till 7 LAT) and late afternoon (17 LAT till Sunset), the recorded values are minimum, with average value during the whole period ranges from 2 to 64 Wh m^{-2}.

(b) Variation of monthly and seasonal averages of daily totals of diffuse solar radiation (D_{ad})

The variation of D_{ad} through the measurement period is graphically represented in *Fig. 2*. The value of D_{ad} fluctuates strongly from day to day according to the corresponding change of the atmospheric conditions (water content, amount of cloud, aerosol particles, etc). It ranges from 4360 Wh m^{-2} at the day number 129 (May 8) to 734 Wh m^{-2} at the day number 345 (Dec 10). The variation of monthly and seasonal averages of D_{ad} is given also in Table 3.

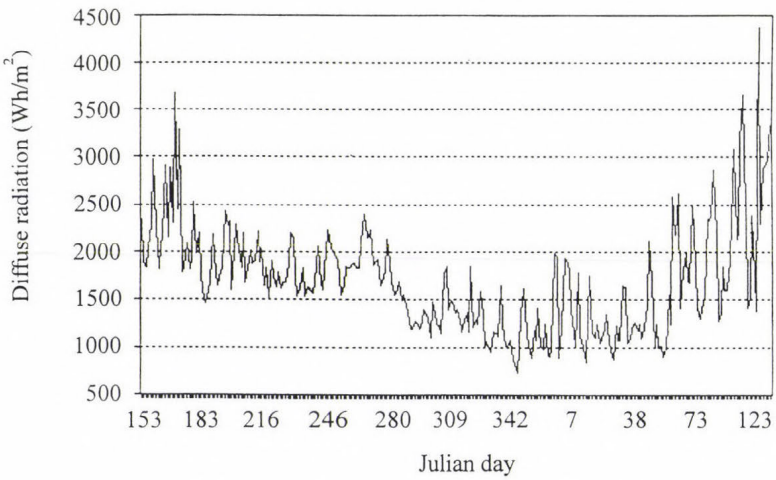

Fig. 2. Variation of daily totals of diffuse solar radiation (June 1992–May 1993) in Qena/Egypt.

(c) Percentage frequency distributions of D_{ad}

The percentage frequency distributions of D_{ad} in the different months, seasons and the whole measurement period are summarized in *Table 4*. The table shows that the percentage frequency of D_{ad} received on a horizontal surface in the study region in the range >4 kWh m^{-2} is very low compared to that of the corresponding global solar radiation (G_{ad}) (see Table 2). About 93.2% of the days in the year have the values of D_{ad} within the low range 0.5–2.5 kWh m^{-2}.

Table 4. Percentage of frequency distribution of daily totals of diffuse solar radiation through the measurement period in Qena/Egypt

Range (Pk Wh/m^{-2})		0.5-1	1-1.5	1.5-2	2-2.5	2.5-3	3-3.5	3.5-4	4-4.5
June	1992	0.0	0.0	34.6	42.3	15.4	3.8	3.8	0.0
July		0.0	8.3	54.2	37.5	0.0	0.0	0.0	0.0
August		0.0	0.0	85.2	14.8	0.0	0.0	0.0	0.0
September		0.0	0.0	64.0	36.0	0.0	0.0	0.0	0.0
October		0.0	69.2	26.9	3.8	0.0	0.0	0.0	0.0
November		12.5	75.0	12.5	0.0	0.0	0.0	0.0	0.0
December		38.5	46.2	15.4	0.0	0.0	0.0	0.0	0.0
January	1993	20.0	60.0	20.0	0.0	0.0	0.0	0.0	0.0
February		17.4	56.5	17.4	4.3	4.3	0.0	0.0	0.0
March		0.0	30.8	38.5	15.4	15.4	0.0	0.0	0.0
April		0.0	14.3	23.8	42.9	4.8	9.5	4.8	0.0
May		0.0	12.5	12.5	12.5	37.5	12.5	0.0	12.5
Summer		0.0	2.6	66.7	28.2	1.3	0.0	1.3	0.0
Autumn		10.8	60.8	24.3	4.1	0.0	0.0	0.0	0.0
Winter		20.9	47.8	22.4	4.5	4.5	0.0	0.0	0.0
Spring		0.0	14.0	20.0	38.0	14.0	8.0	4.0	2.0
Year		8.2	32.1	35.4	17.5	4.1	1.5	0.7	0.4

4.2.2 Comparison between diffuse solar radiation in all (D_a) and cloudless (D_c) sky conditions

The results of diffuse solar radiation measurements in cloudless sky conditions (D_c) are summarized in Table 3. A comparison study has been done between the diffuse solar radiation measured in both all sky (D_a) and cloudless (D_c) sky conditions for investigating to what extent the clouds affect the values of diffuse solar radiation. The following conclusions may be deduced from this table:

(i) The same behaviors are generally observed for the variations of hourly and daily totals (monthly and seasonal averages) of diffuse solar radiation in all sky (D_{ah}, D_{ad}) and cloudless sky conditions (D_{ch}, D_{cd}). However the measured values of D_{ch} and D_{cd} were smaller than those of D_{ah} and D_{ad}, reflecting the influence of clouds in increasing the diffuse solar radiation.

(ii) The average value of D_{ch} over the whole measurement period is maximum at midday hours (11–13 LAT). It has the value 180 Wh m^{-2} ranging from 230 Wh m^{-2} in June to 128 Wh m^{-2} in December, while it is minimum in the early morning (Sunrise-7 LAT) and late afternoon (17 LAT-Sunset) being in some months in the order of the instrument offset.

(iii) The monthly and seasonal average values of D_{cd} were maximum in May (2046 Wh m^{-2}) and spring (2126 Wh m^{-2}), while it is minimum in December (1059 Wh m^{-2}) and winter (1200 Wh m^{-2}). Its average value over the year is 1652 Wh m^{-2}.

(iv) Over the whole period the influence of clouds is not large because the low effect in some months reduce the high one in other months.

4.3 Characteristics of diffuse fraction (k) of global solar radiation

The diffuse fraction is defined as the ratio between the diffuse solar radiation and the global solar radiation, both received on a horizontal surface. Its diurnal and seasonal variations are represented and discussed in the following sections.

4.3.1 All sky conditions measurements (k_a)

(a) Hourly variation of diffuse fraction (k_{ah})

Table 5 summarizes the results of hourly variation of diffuse fraction from sunrise to sunset through the period from June 1992 to May 1993. From this table we can see that k_{ah} decreases from sunrise till midday and then increases again in the direction of sunset.

(b) Variation of daily averages of diffuse fraction of global solar radiation (k_{ad})

The variation of k_{ad} is shown in *Fig. 3*. Its value fluctuates obviously from day to day corresponding to the fluctuation of G_{ad} and D_{ad} discussed in sections 4.1.b and 4.2.b. It ranges from 0.14 (at the day number 56 (Feb 25)) to 0.9 (at the day number 7 (Jan 7)) and is characterized by remarkable fluctuations in the days numbered from 326 to 172, in which k_{ad} value tends to be higher than in the other days of the measurement period. This is evident considering the instability of the atmosphere in these days with respect to water content, dust and clouds, which have also somewhat higher values in these days, as mentioned above. The average values of k_{ad} for each month and season in the measurement period are also given in Table 5. The maximum values of average k_{ad} were observed in May (0.39) as well as in winter and spring (0.31), while the minimum ones were recorded in July & August (0.23) and summer (0.25).

(c) Relation between daily average of diffuse fraction (k_{ad}) and clearness index (k_{td})

The clearness index is defined as the ratio of global solar radiation at the earth's surface (G_a) to extraterrestrial solar radiation (G_0) received on a horizontal surface. The relation between k_{ad} and k_{td} is represented graphically in the scatter plot in *Fig. 4* for all the daily measurements in all sky conditions. The figure shows that:

Table 5. Results of mean values of hourly and daily diffuse fraction at all (K_a) and cloudless (K_c) sky conditions (June 1992–May 1993; in Qena/Egypt)

LAT		Sr-5	5-6	6-7	7-8	8-9	9-10	10-11	11-12	12-13	13-14	14-15	15-16	16-17	17-18	18-SS	Daily total
Jun 1992	K_a	0.78	0.65	0.46	0.34	0.28	0.25	0.23	0.23	0.24	0.24	0.27	0.32	0.43	0.62	0.92	0.28
	K_c	0.78	0.64	0.43	0.32	0.27	0.24	0.22	0.22	0.23	0.24	0.26	0.31	0.42	0.62	0.91	0.27
Jul	K_a	0.79	0.58	0.37	0.28	0.24	0.21	0.19	0.19	0.19	0.20	0.23	0.27	0.35	0.54	0.87	0.23
	K_c	0.79	0.58	0.37	0.28	0.24	0.21	0.19	0.19	0.19	0.19	0.22	0.27	0.35	0.53	0.87	0.23
Aug	K_a		0.61	0.42	0.31	0.23	0.21	0.19	0.18	0.19	0.20	0.23	0.27	0.37	0.57		0.23
	K_c		0.60	0.42	0.31	0.22	0.20	0.18	0.17	0.18	0.19	0.21	0.27	0.37	0.57		0.22
Sep	K_a		0.87	0.54	0.37	0.30	0.26	0.23	0.23	0.23	0.25	0.29	0.36	0.51	0.81		0.28
	K_c		0.87	0.52	0.36	0.29	0.25	0.23	0.22	0.22	0.24	0.28	0.34	0.48	0.81		0.27
Oct	K_a		0.76	0.53	0.35	0.27	0.23	0.21	0.20	0.20	0.22	0.26	0.34	0.50	0.82		0.25
	K_c		0.76	0.54	0.34	0.26	0.23	0.20	0.20	0.20	0.25	0.25	0.33	0.49	0.81		0.24
Nov	K_a			0.71	0.44	0.34	0.27	0.25	0.22	0.24	0.26	0.32	0.42	0.69	0.76		0.29
	K_c			0.70	0.42	0.31	0.26	0.24	0.21	0.22	0.23	0.27	0.39	0.64			0.27
Dec	K_a			0.77	0.48	0.35	0.29	0.25	0.24	0.20	0.26	0.29	0.40	0.64	0.80		0.29
	K_c			0.75	0.45	0.34	0.26	0.23	0.22	0.20	0.21	0.24	0.36	0.61			0.25
Jan 1993	K_a			0.76	0.66	0.42	0.34	0.31	0.28	0.30	0.31	0.35	0.41	0.53	0.69		0.34
	K_c				0.59	0.32	0.25	0.22	0.20	0.20	0.20	0.22	0.26	0.35	0.62		0.23
Feb	K_a			0.68	0.48	0.33	0.28	0.25	0.22	0.21	0.22	0.27	0.28	0.37	0.53	0.78	0.26
	K_c			0.67	0.45	0.30	0.26	0.22	0.18	0.17	0.17	0.20	0.22	0.31	0.49	0.78	0.22
Mar	K_a			0.78	0.53	0.39	0.30	0.26	0.23	0.24	0.26	0.29	0.34	0.43	0.58	0.86	0.29
	K_c			0.79	0.54	0.39	0.30	0.26	0.23	0.23	0.24	0.26	0.31	0.40	0.57	0.86	0.28
Apr	K_a			0.68	0.43	0.52	0.28	0.27	0.27	0.24	0.30	0.33	0.38	0.47	0.60	0.78	0.32
	K_c			0.65	0.43	0.31	0.22	0.20	0.20	0.18	0.20	0.23	0.30	0.37	0.53	0.72	0.25
May	K_a		0.86	0.61	0.39	0.33	0.31	0.35	0.32	0.34	0.48	0.50	0.49	0.58	0.68	0.86	0.39
	K_c		0.86	0.60	0.31	0.21	0.16	0.16	0.15	0.14	0.14	0.18	0.22	0.32	0.56	0.91	0.29
Summer	K_a	0.79	0.65	0.43	0.31	0.25	0.22	0.20	0.20	0.20	0.21	0.24	0.29	0.39	0.60	0.88	0.25
	K_c	0.77	0.63	0.41	0.30	0.24	0.21	0.19	0.19	0.19	0.20	0.23	0.28	0.38	0.59	0.87	0.23
Autumn	K_a		0.82	0.64	0.40	0.31	0.25	0.23	0.22	0.22	0.24	0.28	0.38	0.59	0.83		0.27
	K_c		0.82	0.61	0.39	0.30	0.25	0.22	0.21	0.21	0.23	0.26	0.36	0.56	0.83		0.27
Winter	K_a			0.75	0.57	0.39	0.33	0.28	0.25	0.27	0.28	0.32	0.37	0.49	0.64	0.83	0.31
	K_c			0.73	0.52	0.33	0.26	0.23	0.20	0.19	0.20	0.22	0.25	0.36	0.58	0.82	0.24
Spring	K_a	0.77	0.76	0.59	0.39	0.39	0.27	0.26	0.26	0.25	0.30	0.33	0.37	0.46	0.62	0.88	0.31
	K_c	0.80	0.75	0.55	0.35	0.29	0.23	0.21	0.21	0.21	0.22	0.24	0.30	0.40	0.59	0.83	0.27
Year	K_a	0.78	0.71	0.58	0.42	0.33	0.27	0.24	0.23	0.23	0.25	0.29	0.35	0.49	0.66	0.87	0.28
	K_c	0.79	0.70	0.54	0.38	0.28	0.24	0.21	0.20	0.20	0.21	0.24	0.30	0.43	0.64	0.85	0.25

(i) Most values of diffuse fraction condense at the right lower part of the plot (low k_{ad} and high k_{td}) giving further evidence to the high availability of incoming solar radiation in most of the year in Qena.

(ii) At any value of clearness index k_{td}, there are many values of diffuse fraction k_{ad}, which means that k_{ad} depends on other parameters in addition to k_{td}. The most important parameter is the sun elevation, which plays an active part in this consideration. This conclusion seems to be more clear in view of the not very high correlation found between k_{ad} and k_{td} (correlation coefficient = - 0.68).

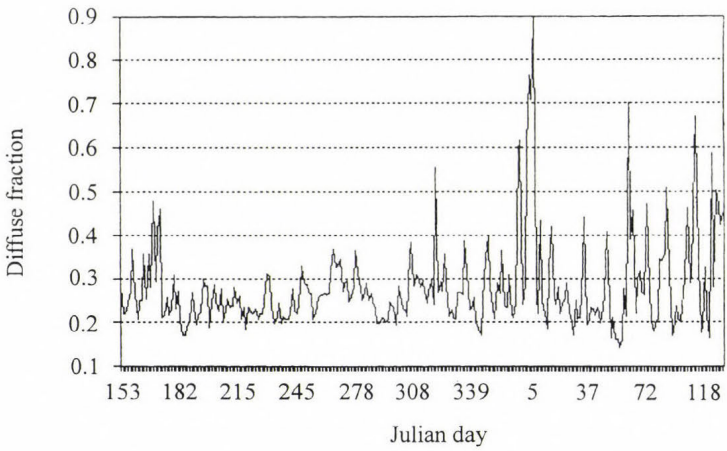

Fig. 3. Variation of daily diffuse fraction (June 1992–May 1993) in Qena/Egypt.

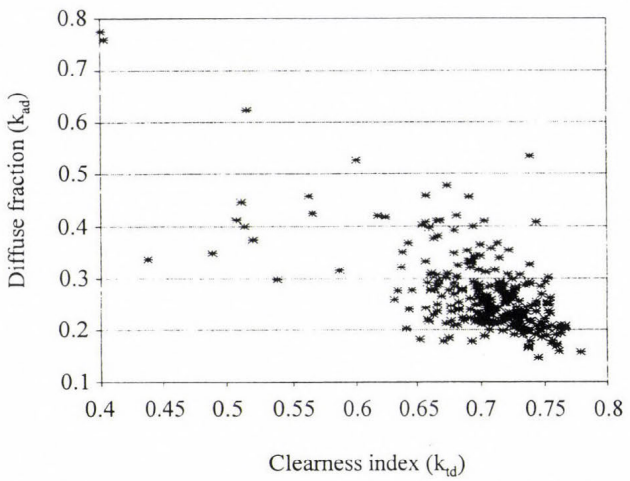

Fig. 4. Relation between daily values of diffuse fraction and clearness index.

4.3.2 Comparison between the diffuse fraction in all (k_a) and cloudless (k_c) sky conditions

Table 5 summarizes the results of k_c through the measurement period. The maximum values of average k_c were observed in March and May (0.28) and spring (0.27), while the minimum ones were recorded in August (0.22), summer (0.23). Considering that the main affecting parameters on k_c are the water vapor and suspended dust particles, the above mentioned variation seems to be explainable in view of the dusty khamaseen wind blowing in the spring months in the study region and leading to high concentrations of aerosols.

4.4 Effect of atmosphere

4.4.1 Effect of cloud

Fig. 5 represents the monthly variation of the G/G_0 and average cloud amount in octas from June 1992 to May 1993. The effect of clouds appears in the higher values of G/G_0 at cloudless days compared to their values at all days measurements. As it is clear in this figure this effect is negligible in the months from June to November and obvious from December to May according to the average amount of clouds observed in these months. It varies from 0.08 octas at July and September to 2.68 octas in May. Most of the clouds were fairly transparent Cirrus (transmissivity $\approx$0.6 to 0.75), except in December to February and some days in April and May, in which As and St types (transmissivity $\approx$0.43 to 0.60) were observed.

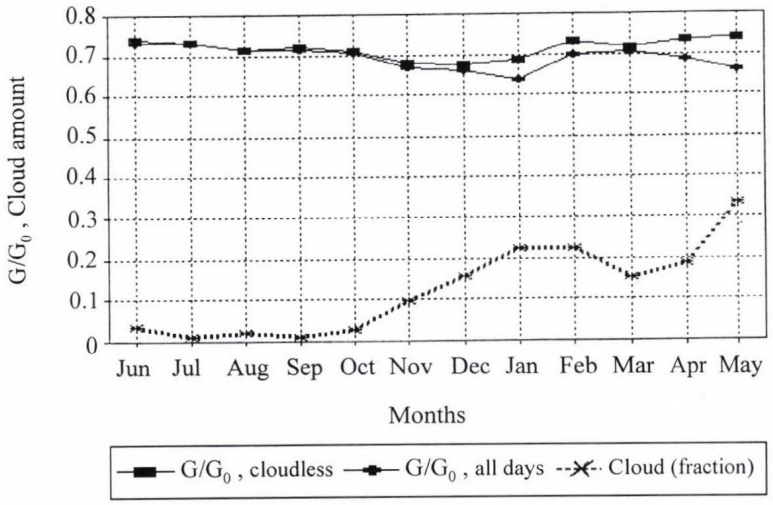

Fig. 5. Effect of clouds on clearness index (G/G_0) in Qena/Egypt.

4.4.2 *Effect of aerosol and water vapor*

Fig. 6 shows the variation of the G/G_0 with the extinction of the incoming solar radiation caused by aerosol a_A and water vapor a_W at cloudless days through the measurement period. This figure shows clearly a high contribution of aerosol dust particles (0.254–0.342) in the reduction of G/G_0 in comparison with that of water vapor (0.118–0.144). This is in a good agreement with the nature of the study region, because Qena is not an industrial district and characterized by a high content of dust particles dispersed from near eastern desert and various human activities (*El-Shazly*, 1989).

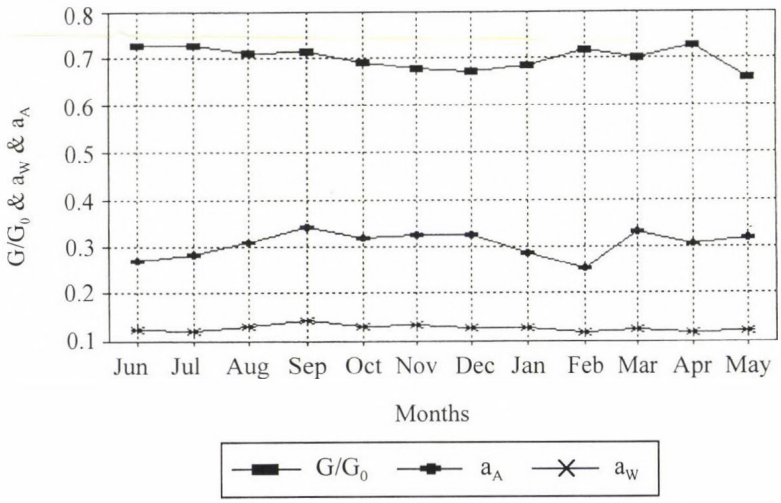

Fig. 6. Effect of aerosols and water vapor on clearness index at cloudless days in Qena/Egypt.

5. Conclusion

(i) The study region receives a considerable quantity of solar energy. 95.6% of the days through the year have values of global solar radiation in the high range of 4–9 kWh m^{-2}, while 96.7% of the days have diffuse solar radiation in the low range from 0.5 to 2.5 kWh m^{-2}.

(ii) The reduction of global solar radiation by clouds represents a small percentage (4.6%), which refers to the low degree of cloudiness in the study region (1 octa in average over the year).

(iii) The relation between the diffuse fraction k_{ad} and clearness index as well the low diffuse fraction indicate the high availability of incoming solar radiation in most of the year.

(iv) Considerable fluctuations of the different solar radiation components were observed in March, April, May and January owing to the high fluctuation of the atmospheric conditions in these months.

(v) The average value of daily total of global solar radiation measured in Qena is comparable with that recorded by Meteorological Authority of A.R. Egypt, 1992 at different locations in Egypt (see *Table 6*).

Table 6. Comparison between the yearly average of daily totals of global solar radiation (G) arriving at horizontal surface in all sky conditions at different locations in Egypt

Location	Qena	Matruh	Tahrir	Cairo	Kharag	Aswan
G(Wh m^{-2})	6289	5525	5294	6394	6416	6416

All these above conclusions indicate that the incoming solar energy at Qena is a significant source of renewable clean energy, which is sufficient to supply people with the necessary energy and encourages us to use it for developing this region, the subject which should be considered in the future.

References

Al-Jamal, K., Ayyash, S., Rasas, M., Al-Aruri, S. and *Shaban, N.*, 1987: Atmospheric turbidity in Kuwait. *Atmospheric Environment 21*, 1855-1859.

Atwater, M.A. and *Ball, J.T.*, 1981 : Effect of clouds on insolation models. *Solar Energy 27*, 37-44.

El-Shazly, S.M., 1989: Studies of the number concentrations and size distribution of the suspended dust particles in the atmosphere of Qena/Egypt. *Water, Air and Soil Pollution* 45, 121-132.

Iqbal, M., 1983: *An Introduction to Solar Radiation*. Academic Press, New York.

Kasten, F., 1966: A new table and approximate formula for relative nnnn optical air mass. *Arch. Meteor. Geophys. Bioklimatol.* Ser. 14, 206-223.

Kudish, A.T., Wolf, D. and *Machlay, Y.*, 1983: Solar radiation for Beer Sheva Israel. *Solar Energy 30*, 33-37.

Kuye, A. and *Jagtap, S.S.*, 1992: Analysis of solar radiation data for port harcourt, Nigeria. *Solar Energy 49*, 139-145.

Latimer, J.R. and *Mac Dowall, J.*, 1971: Radiation measurement, International field year for the great lakes. *Technical Manual Series*, No. 2.

Leckner, B., 1978: The spectral distribution of solar radiation at the earth's surface. Elements of the model. *Solar Energy 20*, 143-150.

Moriarity, W.W., 1991: Estimation of diffuse from measured global solar radiation. *Solar Energy 47*, No. 2, 75-82.

Morris, N., James, G.E. and *William, D.B.*, 1982: *Understanding our Atmospheric Environment*. W.H. Freeman Company, San Francisco.

Neuwirth, F., 1980: The estimation of global and sky radiation in Austria. *Solar Energy 24*, 421-426.

World Meteorological Organization (WMO), 1983: Guide to Meteorological Instruments and Method of Observation. Geneva, Switzerland.

NEWS

Academy Prize for hydrologists

The Hungarian Academy of Sciences (Budapest) awarded a joint prize on the CLX. General Assembly in May 1997 to *Ödön Starosolszky* Civ. Eng., member of the editorial board of IDŐJÁRÁS and to *Károly Szesztay* Civ. Eng., the wellknown Hungarian hydrologist for the development of the principles of the environmental hydrology and hydraulics, for the establishment of the environmentally sound water management and for the promotion of application of scientific results on international scale. During the awarding ceremony considerable emphasis was given to the comprehensive report "The impact of climate change on hydrological and water-quality parameters" submitted by the team leader, Ö. Starosolszky in 1994 to the Hungarian National Science Foundation.

Dr. Ö. Starosolszky is a member of the editorial board of IDŐJÁRÁS since 1986 and wellknown not only among hydrologists, but among meteorologists as well. He is particularly appreciated due to his activity in the World Meteorological Organization. Among others, he was co-author and editor of the following WMO publications: Hydrology of Disasters (1989), Hydrological Aspects of athe Accidental Water Pollution (1993), the National Capabilities for the Assessment of Water Resources (1996). He was co-director of two NATO meetings "Flood Defence" Advance Study Institute (1994) and "Controversies between Water Resources Development and the Environment" Advance Research Workshop (1996), and editor of the relevant publications. He contributed to IAHR seminars on ecohydraulics (Utrecht, 1991, and Trondheim, 1994).

As president of the Commission for Hydrology of WMO (1984–93) and vice-president of IAHIR he acted, as chairman or general reporter on several international meetings. He was member of WG-II of the Intergovernmental Panel on Climate Change, lead author for the theme of Hydrology (1995). He participated in a PECO project of the European Union for climate change impact on the European water resources. In the last six years he was chairman of the Committee on Water Science of the Hungarian Academy of Sciences.

The name of *Dr. K. Szesztay* sounds very well in the meteorological community. He wrote several studies in the last four decades on the heat and water budget of the Carpathian-Basin, and about the evaporation of free water surface. On the other hand, he is an internationally wellknown expert of the Hungarian water management, who participated in the organisation of the UN

Water Conference (Mar del Plata, 1977). He had great merits in the formulation of the conference report. He served more than 6 years in New York at the UN headquarters, as senior expert. He was the president of the international Association for Hydrological Sciences (IAHS). During his career he devoted several years to the scientific base of the hydrological forecasts, the water demand of the vegetation, the long-term planning of water resources, including the third Water Resources Master-Plan of Hungary. In the last years his major interest was paid to the identification of the environmental aspects in the water management. The award was also justified by his book on the "Finite Tolerance of our Planet" (Akadémiai Kiadó, 1992, Budapest), where he analyzed the technical development and the change of the global environment with regard to the tolerance of the Earth. He went beyond the basic problems of the water management, since he attempted to quantify the general problem of the water economy. His latest outstanding work is his comprehensive review on the effect of climate change on the water quality.

The Editorial Board wishes both awarded experts further success and fruitful collaboration with the meteorologists.

E. Antal

ATMOSPHERIC ENVIRONMENT

an international journal

To promote the distribution of Atmospheric Environment *Időjárás* publishes regularly the *contents* of this important journal. For further information the interested reader is asked to contact *Prof. P. Brimblecombe,* School for Environmental Sciences, University of East Anglia, Norwich NR4 7TJ, U.K.; E-mail: atmos_env@uea.ac.uk

Volume 31 Number 10 1997

Volume 31 Number 11 1997

Volume 31 Number 12 1997

Aeronox: Atmospheric impact of NO_x emissions From aircraft

Volume 31 Number 13 1997

NOTES TO CONTRIBUTORS

The purpose of *Időjárás* is to publish papers in the field of theoretical and applied meteorology. These may be reports on new results of scientific investigations, critical review articles summarizing current problems in certain subject, or shorter contributions dealing with a specific question. Authors may be of any nationality but papers are published only in English.

Papers will be subjected to constructive criticism by unidentified referees.

* * *

The manuscript should meet the following formal requirements:

Title should contain the title of the paper, the names(s) of the author(s) with indication of the name and address of employment.

The title should be followed by an *abstract* containing the aim, method and conclusions of the scientific investigation. After the abstract, the *key-words* of the content of the paper must be given.

Three copies of the manuscript, typed with double space, should be sent to the Editor-in-Chief: *P.O. Box 39, H-1675 Budapest,* Hungary.

References: The text citation should contain the name(s) of the author(s) in Italic letter or underlined and the year of publication. In case of one author: *Miller* (1989), or if the name of the author cannot be fitted into the text: *(Miller,* 1989); in the case of two authors: *Gamov* and *Cleveland* (1973); if there are more than two authors: *Smith et al.* (1990). When referring to several papers published in the same year by the same author, the year of publication should be followed by letters a,b etc. At the end of the paper the list of references should be arranged alphabetically. For an article: the name(s) of author(s) in Italics or underlined, year, title of article, name of journal, volume number (the latter two in Italics or underlined) and pages. E.g. *Nathan, K. K.,* 1986: A note on the relationship between photosynthetically active radiation and cloud amount. *Időjárás 90,* 10-13. For a book: the name(s) of author(s), year, title of the book (all in Italics or underlined with except of the year), publisher and place of publication. E.g. *Junge, C. E.,* 1963: *Air Chemistry and Radioactivity.* Academic Press, New York and London.

Figures should be prepared entirely in black India ink upon transparent paper or copied by a good quality copier. A series of figures should be attached to each copy of the manuscript. The legends of figures should be given on a separate sheet. Photographs of good quality may be provided in black and white.

Tables should be marked by Arabic numbers and provided on separate sheets together with relevant captions. In one table the column number is maximum 13 if possible. One column should not contain more than five characters.

Mathematical formulas and *symbols:* non-Latin letters and hand-written marks should be explained by making marginal notes in pencil.

The final text should be submitted both in manuscript form and on *diskette.* Use standard 3.5" or 5.25" DOS formatted diskettes for this purpose. The following word processors are supported: WordPerfect 5.1, WordPerfect for Windows 5.1, Microsoft Word 5.5, Microsoft Word 6.0. In all other cases the preferred text format is ASCII.

* * *

Authors receive 30 *reprints* free of charge. Additional reprints may be ordered at the authors' expense when sending back the proofs to the Editorial Office.

Published by the Hungarian Meteorological Service

Budapest, Hungary

INDEX: 26 361

HU ISSN 0324-6329